Bloch equations in terahertz magnetic-resonance ellipsometry

Viktor Rindert , 1,2,3,* Steffen Richter , 1,2 Philipp Kühne , 4,5,6 Alexander Ruder, Vanya Darakchieva , 1,2,3,4 and Mathias Schubert , 1,2,7

1 NanoLund and Solid State Physics, Lund University, S-22100 Lund, Sweden

2 Terahertz Materials Analysis Center, THeMAC, Lund University, S-22100 Lund, Sweden

3 Center for III-Nitride Technology, C3NiT - Janzén, Lund University, S-22100 Lund, Sweden

4 Department of Physics, Chemistry, and Biology (IFM), Linköping University, SE 58183, Linköping, Sweden

5 Terahertz Materials Analysis Center, THeMAC, Linköping University, SE 58183, Linköping, Sweden

6 Center for III-Nitride Technology, C3NiT - Janzén, Linköping University, SE 58183, Linköping, Sweden

7 Department of Electrical and Computer Engineering, University of Nebraska-Lincoln, Lincoln, Nebraska 68588, USA



(Received 22 April 2024; revised 10 July 2024; accepted 17 July 2024; published 7 August 2024)

A generalized approach derived from Bloch's equation of motion of nuclear magnetic moments is presented to model the frequency, magnetic field, spin density, and temperature dependencies in the electromagnetic permeability tensor for materials with magnetic resonances. The resulting tensor model predicts characteristic polarization signatures which can be observed, for example, in Mueller matrix element spectra measured. When augmented with thermodynamic considerations and suitable Hamiltonian description of the magnetic eigenvalue spectrum, important parameters such as density, spectral amplitude distribution, relaxation time constants, and geometrical orientation parameters of the magnetic moments can be obtained from comparing the generalized model approach to experimental data. We demonstrate our approach by comparing model calculations with full Mueller matrix element spectra measured at an oblique angle of incidence in the terahertz spectral range, across electron spin resonance quintuplet transitions observed in wurtzite-structure GaN doped with iron. Our model correctly predicts the complexity of the polarization signatures observed in the 15 independent elements of the normalized Mueller matrix for both positive and negative magnetic fields and will become useful for future analysis of frequency and magnetic field-dependent magnetic resonance measurements.

DOI: 10.1103/PhysRevB.110.054413

I. INTRODUCTION

Magnetic resonance spectroscopy stands as a cornerstone in the realm of molecular and materials research. Originating from the seminal observations by Zeeman on the impact of magnetic fields on spectral lines, magnetic resonance spectroscopy has evolved into a comprehensive suite of techniques, including nuclear magnetic resonance (NMR), electron paramagnetic resonance (EPR), and ferromagnetic resonance (FMR). These methodologies have provided unparalleled insights into molecular structures, and dynamics, significantly advancing our understanding across chemistry, materials science, medicine, and semiconductor physics. EPR is widely used to study quantum transitions of molecular magnetic moments [1]. Conventional EPR instruments detect magnetic resonance at a few fixed frequencies, typically at a few tens of GHz [2]. The Zeeman splitting energy, ΔE , of a free electron at 10 GHz, for example, corresponds to a magnetic field of $B = \frac{\Delta E}{g\mu_B} = 357$ mT, and vacuum wavelength

Published by the American Physical Society under the terms of the Creative Commons Attribution 4.0 International license. Further distribution of this work must maintain attribution to the author(s) and the published article's title, journal citation, and DOI. Funded by Bibsam.

of $\lambda \approx 3$ cm, where $\mu_B = \frac{e\hbar}{2m_e}$ is the Bohr magneton, e is the unit electric charge, \hbar is the reduced Planck constant, and m_e is the free electron mass. Pioneered by Felix Bloch in his seminal 1946 paper [3], electromagnetic absorbance loss measurements of magnetic transitions are typically performed in resonator cavities at fixed frequencies under near-field conditions and slowly scanning external magnetic field permitting for relatively small sample size and highly sensitive detection. Historically, thus conventional EPR practice is positioning the sample within a resonant microwave cavity. While effective for certain applications, this setup inherently imposes a restriction on the system, confining it to a finite set of discrete frequencies. This limitation has traditionally hindered the ability to fully explore frequency-dependent magnetic suscetibility characteristics [4]. Tuning frequency or modifying polarization in such resonator geometries is difficult, however, investigating magnetic resonances at larger magnetic fields is generally desirable since energy and magnetic field resolutions improve. At 100 GHz, $\lambda \approx 3$ mm and a magnetic field of B = 3.57 T are needed for the single free electron Zeeman splitting to match. Such magnetic fields can be conveniently achieved with superconducting magnets. Studies of magnetic properties at higher magnetic fields are of interest for large and complex magnetic systems [5,6], for systems with large spin quantum numbers and strong spin-spin coupling [7,8], and for more comprehensive investigations of defect properties in wide-bandgap semiconductors, e.g., in

^{*}Contact author: viktor.rindert@ftf.lth.se

SiC [9–11] and GaN, and in ultrawide-band-gap semiconductors, e.g., AlN [12,13], or gallium oxide [14–21].

In recent years, several groups have developed new methods of performing EPR at higher magnetic fields with the possibility of tuning the frequency used [5,22-25]. Transitioning the resonance conditions into the THz range, far-field optical techniques such as spectroscopic ellipsometry become available. In addition to frequency variation with few-kHz resolution capability, frequency multiplication of highly polarized solid-state synthesizer sources have become available recently as well. Implementing suitable polarization modulation, THz spectroscopic ellipsometry was developed lately, permitting measurement of Mueller matrix spectra [26,27]. Thereby, the anisotropic THz optical properties of samples with complex layer structures and low-symmetry crystal structures can be assessed and quantified. THz ellipsometry was also demonstrated on samples immersed in strong magnetic fields within superconducting split-coil Helmholtz-type magnets for measurement of the optical Hall effect [26–28]. Such measurements can be performed in reflection and transmission geometries and have demonstrated sensitivity to free charge carrier properties such as effective mass, mobility, density, and sign (electron, hole). Employing the advantages of free space propagation such as freely tunable frequency, free choice of propagation direction, and, most importantly, variation of all possible polarization conditions, THz EPR ellipsometry permits investigations of magnetic transitions, including their energy-magnetic field diagrams as well as their polarization properties [29,30]. THz EPR thereby dispenses with the need for resonance cavities and permits the study of semiconductor heterostructures and thin films. Frequencymagnetic field maps allow investigators to quickly identify the origins of observed transitions because different mechanisms, such as hyperfine structure splitting, Zeeman splitting, or zero-field splitting, reveal different frequency-field diagrams [5]. Also, level populations change with magnetic field and, therefore, with frequency and reveal dynamics in the complex-valued spin susceptibility, which can be measured using ellipsometry [1,31].

The previously developed THz Optical Hall effect instrumentation is readily available for THz EPR ellipsometry measurements. Magnetic field and frequency dependent linearly and circularly polarized Mueller matrix element spectra were measured of the magnetic spin transitions associated with cubic and hexagonal lattice site nitrogen impurities in 4H-SiC [29]. In our recent work, we have reported magnetic field-scanning THz-EPR ellipsometry measurements at selected frequencies of transitions associated with iron impurities in β -Ga₂O₃ [32] The high-spin S = 5/2 state of Fe³⁺ causes five transitions which were all detected simultaneously, in contrast to conventional low-field EPR. Analysis of the ellipsometry data, based on direct lineshape matching to the Mueller-matrix elements, resulted in the full set of fourth-order monoclinic zero-field splitting parameters for the octahedrally and tetrahedrally coordinated defects. A subsequent Hamiltonian analysis revealed that simplified second-order orthorhombic approximations are insufficient to model the high-spin system at high magnetic fields owing to the monoclinic symmetry of the host crystal [32].

Ellipsometry is a method for accurately characterizing the linear optical properties of materials, particularly of thin films [33]. Data analysis requires model calculations which consider plane wave propagation throughout the sample including Fabry-Perot interference, and requires appropriate assumptions about the complex-valued dielectric (ε) and magnetic (μ) material functions within Maxwell's equations, $\mathbf{D} =$ $\varepsilon_0 \varepsilon \mathbf{E}$, and $\mathbf{B} = \mu_0 \mu \mathbf{H}$, where **D** and **E**, and **B** and **H** are dielectric displacement and electric field phasors, and magnetic induction and magnetic field phasors, respectively. Both response functions are second-rank tensors and are complexvalued. The structure of the tensors reveals the underlying physical polarization processes that lead to the optical response of a given system. It is commonly accepted for optical frequencies that the permeability μ is unity and isotropic, independent of frequency and wave vector. However, at THz frequencies across magnetic transitions, the magnetic susceptibility can differ significantly from unity. This was demonstrated in our previous work reporting the magnetic field- and frequency-scanning THz-EPR ellipsometry measurement of the Nitrogen impurity in SiC [29]. The prototype in-house built THz-EPR ellipsometery instrument at the THz Materials Analysis Center used in this work measures the complete Mueller matrix in the THz spectral range with freely tunable frequency at a spectral resolution of approximately 50 kHz, for example, in the 200 to 210 GHz region. The availability of the full Mueller matrix spectra offers new access to detailed sample polarization properties and the underlying physical mechanisms using appropriate model calculations.

In order to perform model analysis to obtain accurate quantitative physical parameters in ellipsometry, a suitable model must be selected. For dielectric processes, such models are referred to as model dielectric function (MDF) approaches which are then used to identify, for example, band-to-band transition energies, or phonon modes and their eigendielectric polarization directions [33-35]. An eigendielectric displacement vector summation approach was presented recently for polar vibrations in materials with arbitrary crystal symmetry systems, which was derived from the microscopic Born-Huang description of polar lattice vibrations in the harmonic approximation [36]. This eigendielectric polarization or eigenpolarization model was later applied to detailed analyses of phonon mode properties on monoclinic crystal, for example, in gallium oxide [34], cadmium tungstate [35], yttrium orthosilicate [37], and also in orthorhombic neodymium gallate [38]. This eigenpolarization model also permitted to provide a detailed understanding of the effects of the so-called directional modes in the Born-Huang model and the peculiar order of the transverse and longitudinal phonon modes in polar crystals with monoclinic symmetry [39], as well as the mechanisms of coupling with free charge carriers [40]. A significant feature of this eigenpolarization model is the existence of a vector, an eigenpolarization vector, which represents the direction of the dipole oscillation. These MDF approaches are derived and founded on physical models and fundamental principles of classical and quantum mechanics including energy, charge, and momentum conservation. However, ad hoc model functions are often used, which lack rigorous physical derivations. For analysis of our previous THz-EPR ellipsometry data [29], such an ad hoc model was

implemented. This model sufficed to reproduce the main features of the ellipsometry spectra. However, other characteristic measured properties did not correspond well with the ad hoc model. Previous model descriptions that correctly render the complex-valued frequency and external magnetic field dependencies for the tensor appearance of the magnetic susceptibility for spin or general magnetic transitions are not known from ellipsometry investigations. Hence, such model descriptions must be searched for and tested. In this paper, we present a derivation of a permeability tensor that describes the full magneto-optic response of a material and sufficiently explains THz EPR ellipsometry data for spin transitions. We derived this model from the Bloch equations [3] of the magnetic induction under the influence of an external static and high-frequency magnetic field. We find a model that is similar in structure to the Born-Huang model where magnetic instead of dielectric eigenpolarization directions and eigenfunctions are defined which produce the appearance of the permeability tensor and can be used in summations over multiple magnetic processes. We believe this model will also become useful for analysis of the frequency and magnetic field dependent responses of general magnetic transitions and excitations.

The Bloch equations [3] describe the time evolution of a macroscopic ensemble of magnetic moments by phenomenologically introducing relaxation times. The "Bloch susceptibility" is the form of the magnetic susceptibility derived from the Bloch equations. As the signal strength is proportional to the magnetization, the imaginary part of the Bloch susceptibility is often used to describe absorption spectra within the fields of EPR and nuclear magnetic resonance (NMR) [41–46]. By deconvoluting the lineshape, the relaxation times of the studied magnetic moments can be obtained. These relaxation times are intricately linked to the local interactions of paramagnetic centers with their surrounding environment, and yield information regarding the studied system's electronic structure and molecular motions [47]. The absorption spectra obtained by conventional EPR are in arbitrary units. Analysis of information related to absolute amplitude requires great care. This can be done by using a reference sample with a known spin volume concentration or by studying polarization effects rather than intensity as performed in this study. Once obtained, the amplitude of an EPR signature can be related to the longitudinal relaxation time and the spin volume concentration.

Our work here aims to rigorously evaluate the efficacy of employing the Bloch equation formalism for interpreting magnetic resonance data, specifically obtained through Mueller matrix ellipsometry [33,48–50]. The original Bloch equations, while proficient in providing a fundamental and intuitive framework for understanding the rate processes inherent in magnetic resonance phenomena, frequently fall short in precisely replicating experimental outcomes. This discrepancy arises primarily due to the oversimplified nature of the phenomenological relaxation times, which inadequately capture the complex dynamics of magnetic moments, particularly in scenarios where there is significant interaction and interconversion among them. Here, we demonstrate the validity of the Bloch model by robust agreement between measured and best-match model calculated Mueller matrix spectra for impurity-induced electron spin resonance transitions in Fe-doped GaN as an example. The zero-field splitting parameters of the S=5/2 high-spin impurity $\mathrm{Fe^{3+}}$ in GaN have been investigated previously with fixed frequency low-magnetic field EPR [51]. The frequency-dependent measurements at fixed magnetic fields revealed in this work demonstrate the new capabilities of THz EPR ellipsometry to directly infer spin parameters from individual spectra. In addition, the spin Hamiltonian parameters can be determined from analysis of the eigenvalue spectrum at fixed magnetic fields.

In Sec. IIB, we present the derivation of the frequencydependent complex-valued Bloch susceptibility tensor, which is then expanded to high-spin systems in Sec. II D. Based on the results in Sec. IIB, we demonstrate the structure of the anisotropic magnetic response function tensor and the resulting anisotropic properties. We thereby introduce the Bloch eigenmagnetic polarizability functions and eigenvectors in Sec. II E. These functions establish the base of the Model Magnetic Function (MMF) approach used in Sec. III C for analysis of THz-EPR ellipsometry measurements performed on Fe-doped GaN. In Sec. III B, we present our THz-EPR ellipsometry method used here. Data reduction and parameter determination are discussed in Sec. III D. Section IV details the results of the analysis for low-density Fe-doped GaN. Line-shape analysis results, including amplitude, broadening, and frequency parameters of the two equivalent GaN lattice sites' zero-field-split spin transition quintuplets, are shown, discussed, and compared with available literature data from low-field, fixed-frequency EPR. We then demonstrate the quantitative determination of the spin density using the results of the MMF analysis in combination with a Brillouin magnetization summation approach. The experiment on the spin S = 5/2 system in GaN is selected for the purpose of demonstration. The Hamiltonian description of the zero-field split system is well known and, thereby, is suitable for the purpose here. For this reason, the spin measurements are performed in a specific orientation of the crystal such that Fe³⁺ in two equivalent sites produce identical spin eigenvalues, and thereby simplify the analysis for improved transparency of our MMF approach implemented here.

II. THEORY

A. Generalized spectroscopic ellipsometry

The results of Mueller-matrix ellipsometry [33] are commonly described by Mueller-Calculus, which is a mathematical framework where Mueller matrices [48]

$$\mathbf{M} = \begin{pmatrix} M_{11} & M_{12} & M_{13} & M_{14} \\ M_{21} & M_{22} & M_{23} & M_{24} \\ M_{31} & M_{32} & M_{33} & M_{34} \\ M_{41} & M_{42} & M_{43} & M_{44} \end{pmatrix}, \tag{1}$$

operate on Stokes vectors [33]

$$S = \begin{pmatrix} I_p + I_s \\ I_p - I_s \\ I_{45^{\circ}} - I_{-45^{\circ}} \\ I_{RCP} - I_{1CP} \end{pmatrix}, \tag{2}$$

where s, p, $\pm 45^{\circ}$ denote linearly polarized light perpendicular, parallel, $\pm 45^{\circ}$ to the plane of incidence, while RCP and LCP denote right and left circularly polarized light, respectively. As such, Mueller matrices connect the incident (S_{input}) and emergent (S_{output}) Stokes vectors after transmission through or reflection of a sample

$$S_{\text{output}} = M_{\text{sample}} S_{\text{input}}.$$
 (3)

Specifically, M_{sample} is measured using Mueller matrix ellipsometry. How we compute Mueller matrices is detailed in Appendix A.

B. Bloch susceptibility

To predict the frequency dependence of the complex-valued permeability tensor for a set of magnetic resonances, a model based on the Bloch equations is derived. The set of Bloch equations describes how a magnetization vector $\mathbf{M} = (M_x, M_y, M_z)$ responds to an external perturbation when subjected to a static or slow-changing magnetic induction field B_0 . The magnetic moment associated with the magnetization vector is thought of a continuum density, and may be interpreted as caused by a homogeneous distribution of infinitely small magnetic objects with volume (spin) density n_s . Without loss of generality, with B_0 oriented along direction z, the Bloch equations including the phenomenological relaxation times are represented as follows [52,53]:

$$\frac{\partial M_x}{\partial t} = -\omega_0 M_y - \frac{M_x}{T_2},$$

$$\frac{\partial M_y}{\partial t} = \omega_0 M_x - \frac{M_y}{T_2},$$

$$\frac{\partial M_z}{\partial t} = -\frac{M_z - M_0}{T_1},$$
(4)

where $\omega_0 = \gamma_e B_0$ is the classical Larmor frequency, γ_e is the gyromagnetic ratio, M_0 is the dc magnetization along the z axis and is assumed to be linearly proportional to B_0 , T_1 is the longitudinal relaxation time, and T_2 is the transverse relaxation time. To assess the response of vector M to an oscillating magnetic induction field, i.e., a time-harmonic external perturbation due to an electromagnetic plane wave traversing a magnetized medium, it is advantageous to employ a rotating frame of reference with an identical angular frequency ω as that of the oscillating magnetic field. Moreover, assuming that the oscillating magnetic field is comprised of left-circularly polarized (LCP) light whose oscillating amplitude $H_1 = \frac{1}{\mu_0} B_1$ (CGS units are used throughout this derivation, resulting in $H_1 = B_1$) then remains fixed along the x axis within the rotating frame, where μ_0 is the vacuum permeability and H_1 (B_1) is the auxiliary magnetic (induction) field, the Bloch equations transform into

$$\frac{\partial \tilde{M}_x}{\partial t} = -(\omega_0 - \omega)\tilde{M}_y - \frac{\tilde{M}_x}{T_2},$$

$$\frac{\partial \tilde{M}_y}{\partial t} = (\omega_0 - \omega)\tilde{M}_x - \frac{\tilde{M}_y}{T_2} - \gamma_e B_1 M_z,$$

$$\frac{\partial M_z}{\partial t} = -\frac{M_z - M_0}{T_1} + \gamma_e B_1 \tilde{M}_y,$$
(5)

where " \sim " annotates components of **M** in the rotating frame around the z axis. Solving (5) for a steady-state expression while assuming very large longitudinal relaxation time T_1 yields [52]

$$\tilde{M}_{x} = \chi_{0} T_{2} \omega_{0} \frac{(\omega_{0} - \omega) T_{2}}{1 + T_{2}^{2} (\omega_{0} - \omega)^{2}} B_{1},
\tilde{M}_{y} = \chi_{0} T_{2} \omega_{0} \frac{1}{1 + T_{2}^{2} (\omega_{0} - \omega)^{2}} B_{1},
M_{z} = M_{0},$$
(6)

where we have assumed that $B_1 \ll B_0$, which is typically the case, and we introduce the dc susceptibility $\chi_0 = M_0/B_0$. We can thus express frequency-dependent susceptibility functions χ' and χ'' in the rotating frame of reference

$$\chi'(\omega) = \frac{\tilde{M}_x}{B_1} = \chi_0 T_2 \omega_0 \frac{(\omega_0 - \omega) T_2}{1 + T_2^2 (\omega_0 - \omega)^2},$$

$$\chi''(\omega) = \frac{\tilde{M}_y}{B_1} = \chi_0 T_2 \omega_0 \frac{1}{1 + T_2^2 (\omega_0 - \omega)^2}.$$
(7)

We consider the magnetization response to a left-handed circularly polarized (LCP, +) electromagnetic plane wave and seek the complex-valued frequency-domain Bloch susceptibility $\chi_{B,+} \equiv \chi_1 + i\chi_2$ in the static reference frame. The amplitude of the oscillating induction component of the electromagnetic field in the x direction can be expressed as $B_x = B_1 e^{-i\omega t}$ when the plane wave is propagating along the positive direction of the z axis. Consequently,

$$M_x = \Re(\chi_{B,+} B_1 e^{-i\omega t})$$

= $B_1(\chi_1 \cos(\omega t) + \chi_2 \sin(\omega t)),$ (8)

where \Re denotes the real part. We then express the magnetization through the components in the rotating frame

$$M_x = \tilde{M}_x \cos \omega t + \tilde{M}_y \sin(\omega t)$$

= $B_1(\chi' \cos(\omega t) + \chi'' \sin(\omega t)),$ (9)

and by comparison with Eq. (8)

$$\chi_{B,+} = \chi'(\omega) + i\chi''(\omega), \tag{10}$$

or equivalently

$$\chi_{B,+}(\omega) = \chi_0 \frac{\omega_0}{\omega_0 - \omega - i/T_2}.$$
 (11)

It is noteworthy that the foregoing derivation assumes a positive-valued static induction field, enabling LCP light to drive spin transitions, and resulting in the observed magnetization

$$M_{x} = (\chi' \cos(\omega t) + \chi'' \sin(\omega t))B_{1},$$

$$M_{y} = (-\chi'' \cos(\omega t) + \chi' \sin(\omega t))B_{1},$$

$$M_{z} = \chi_{0}B_{0},$$
(12)

which is neatly summarized by the magnetic susceptibility tensor

$$\chi_{M,+} = \frac{1}{2} \begin{pmatrix} \chi_{B,+} & -i\chi_{B,+} & 0\\ i\chi_{B,+} & \chi_{B,+} & 0\\ 0 & 0 & 2\chi_0 \end{pmatrix}, \tag{13}$$

where the third diagonal element highlights the distinct magnetic response along the z-axis. The time-harmonic response of the magnetic induction within the magnetized medium is then obtained from the summation over the vacuum and spin contributions, $\mathbf{B} = \mu_0 (1 + 4\pi \chi_{M,+}) H_1 = \mu_0 \mu_{M,+} H_1$.

Tensor $\chi_{M,+}$ in Eq. (13) represents the optical response for transitions that are induced by LCP light. This polarization state predominantly influences the optical response near resonance frequencies in the presence of positive magnetic fields. To construct a comprehensive tensor encompassing responses for all polarization states, it is essential to augment the response of right-handed circularly polarized (RCP) light [54]. This augmentation is further based on the principle that any polarization state and its response from a given medium can be represented as a superposition of LCP and RCP components. Considering RCP light as the time-reversed analog of LCP light, the response for RCP light can be derived by applying the time-reversal operator to χ_+ [55,56]. In the frequency domain, the time reversal results in the following transformations [57]

$$B_0 \to -B_0, \quad M_0 \to -M_0,$$

 $\chi_0 \to \chi_0, \quad \omega_0 \to -\omega_0.$ (14)

This means that Eq. (11) transforms into

$$\chi_{B,-} = \chi_0 \frac{\omega_0}{\omega_0 + \omega + i/T_2},\tag{15}$$

and Eq. (13) into

$$\chi_{M,-} = \frac{1}{2} \begin{pmatrix} \chi_{B,-} & i\chi_{B,-} & 0\\ -i\chi_{B,-} & \chi_{B,-} & 0\\ 0 & 0 & 2\chi_0 \end{pmatrix}, \tag{16}$$

when considering the response of RCP light as opposed to LCP light.

The magnetic susceptibility tensor χ_M which renders the optical response for all magnetic field directions is the sum of $\chi_{M,+}$'s and $\chi_{M,-}$'s transverse components

$$\chi_{M} = \frac{1}{2} \begin{pmatrix} \chi_{B,+} + \chi_{B,-} & -i[\chi_{B,+} - \chi_{B,-}] & 0\\ i[\chi_{B,+} - \chi_{B,-}] & \chi_{B,+} + \chi_{B,-} & 0\\ 0 & 0 & 2\chi_{0} \end{pmatrix}. (17)$$

With Eqs. (11) and (15) we can express the on-diagonal and off-diagonal components of χ_M in the frequency domain

$$\chi_{M,xx} = \chi_{M,yy} = 2\chi_0 \frac{\omega_0^2}{\omega_0^2 - \omega^2 - 2i\omega/T_2},$$
(18)

$$\chi_{M,xy} = -\chi_{M,yx} = i2\chi_0 \frac{\omega_0 \omega}{\omega_0^2 - \omega^2 - 2i\omega/T_2}.$$
(19)

Equations (18) and (19) are central to the further discussions in this work. It is noted that the on-diagonal components are equal. Their frequency dependence is identical to that of a harmonically broadened Lorentzian oscillator model. This is no surprise since the Bloch equations describe the motion

of a magnetic moment in a harmonic potential. The offdiagonal components differ in sign and are purely imaginary in case of infinite relaxation time T_2 . Hence, the off-diagonal components render circular dichroism, and when $T_2 < \infty$, the off-diagonal components also describe circular birefringence. The spectral behavior between on- and off-diagonal components is almost identical if $\omega \approx \omega_0$; however, it differs distinctly when $\omega \to 0$ or $\omega \to \infty$. Specifically, the off-diagonal components vanish towards infinite wavelengths, while the on-diagonal components approach χ_0 , the dc magnetic susceptibility. Both components approach zero at high frequencies. A further interesting feature of this model is the fact that the on-diagonal components do not change sign with reversal of the external induction field, B_0 , while the off-diagonal terms do. This phenomenon was noted previously during analysis attempts of THz EPR ellipsometry measurements using an ad-hoc model approach, which failed to explain the observed sign changes in Mueller matrix elements upon magnetic field reversal [29]. Finally, it can be shown that Eqs. (18) and (19) always lead to loss and no gain for $0 \leqslant T_2$, regardless of direction of external induction B_0 and choice of polarization.

To construct the full permeability tensor, we consider the external induction field parallel direction z, and $M_z = M_0 = \chi_0 B_0$, then

$$\mu_{M} = 1 + 4\pi \chi_{M}$$

$$= \begin{pmatrix} 1 + 4\pi \frac{\chi_{0}\omega_{0}^{2}}{\omega_{0}^{2} - \omega^{2} - 2i\omega/T_{2}} & -i4\pi \frac{\chi_{0}\omega_{0}\omega}{\omega_{0}^{2} - \omega^{2} - 2i\omega/T_{2}} & 0\\ i4\pi \frac{\chi_{0}\omega_{0}\omega}{\omega_{0}^{2} - \omega^{2} - 2i\omega/T_{2}} & 1 + 4\pi \frac{\chi_{0}\omega_{0}^{2}}{\omega_{0}^{2} - \omega^{2} - 2i\omega/T_{2}} & 0\\ 0 & 0 & 1 + 4\pi \chi_{0} \end{pmatrix}.$$
(20)

C. Bloch permeability eigenfunction μ_{Rl}

The Bloch permeability μ_{Bl} is introduced as the determinant of the permeability tensor which yields

$$\mu_{\text{BI}} = 1 + 4\pi \, \chi_{M,xx} = 1 + 8\pi \, \chi_0 \frac{\omega_0^2}{\omega_0^2 - \omega^2 - 2i\omega/T_2}.$$
 (21)

Note that $\chi_{M,xx}$ does not change sign upon change of the magnetic field direction. Therefore, $\mu_{\rm Bl}$ does not depend on the external magnetic field direction. Furthermore, the permeability tensor can now be written in the following form:

(18)
$$\mu_{M} = \frac{1}{2} \begin{pmatrix} 1 + \mu_{Bl} & i\frac{\omega}{\omega_{0}}(1 - \mu_{Bl}) & 0 \\ -i\frac{\omega}{\omega_{0}}(1 - \mu_{Bl}) & 1 + \mu_{Bl} & 0 \\ 0 & 0 & \frac{1}{2}(1 + 4\pi\chi_{0}) \end{pmatrix},$$
(22)

and we obtain that μ_{Bl} is indeed eigenfunction to the magnetic component of the electromagnetic wave for LCP (RCP) light at frequencies close to resonance ω_0 ($-\omega_0$), which is easily confirmed by multiplying the tensor with an LCP (RCP)

magnetic field phasor $H_{+} = (1, i, 0)^{T} (H_{-} = (1, -i, 0)^{T})$

$$B = \mu_{M} H_{\pm} = \frac{1}{2} \begin{pmatrix} 1 + \mu_{Bl} & i \frac{\omega}{\omega_{0}} (1 - \mu_{Bl}) & 0 \\ -i \frac{\omega}{\omega_{0}} (1 - \mu_{Bl}) & 1 + \mu_{Bl} & 0 \\ 0 & 0 & \frac{1}{2} (1 + 4\pi \chi_{0}) \end{pmatrix} \begin{pmatrix} 1 \\ \pm i \\ 0 \end{pmatrix} |_{\omega \to \pm \omega_{0}}$$

$$\approx \frac{1}{2} \begin{pmatrix} 1 + \mu_{Bl} & \pm i (1 - \mu_{Bl}) & 0 \\ \mp i (1 - \mu_{Bl}) & 1 + \mu_{Bl} & 0 \\ 0 & 0 & \frac{1}{2} (1 + 4\pi \chi_{0}) \end{pmatrix} \begin{pmatrix} 1 \\ \pm i \\ 0 \end{pmatrix} = \mu_{Bl} H_{\pm}. \tag{23}$$

As such, considering only one circular polarization mode, the scalar function $\mu_{\rm Bl}$ can be sufficient to represent the optical response at frequencies close to the resonant frequencies. $\mu_{\rm Bl}$ is measured and modeled in this work here and will be discussed in Sec. IV. Note specifically that $\mu_{\rm Bl}$ is eigenfunction near resonance for LCP at positive magnetic field B_0 and eigenfunction for RCP at negative magnetic field B_0 . At resonance, the permeability response is unity both for RCP at positive field and for LCP at negative magnetic field. At frequencies outside resonance, the behavior of the permeability is more complex, and this will be discussed below in Sec. II E. Note that the polarization of the light is also affected by the dielectric tensor. The calculation of the polarization state of the propagating electromagnetic waves within the material is discussed in Appendix A.

D. Bloch model extrapolated to high-spin systems

The Bloch model, originally formulated on a rate equation for a two-level system, presents limitations when applied directly to a high-spin system with 2S + 1 levels. Effectively, this results in 2S distinct EPR active species corresponding to the 2S spin projections with the lowest energy. Consequently, the rate equations need to be modified if there is any interconversion between the species [53] by, for instance, utilizing the Bloch-McConnell equations. We still motivate using the simple Bloch model as we operate under the condition $B_1 \ll B_0$, resulting in minimal interconversion by photon absorption. Furthermore, we assume an absence of interactions between the constituent spins within the system as the sample is weakly doped. Effectively, this means that each spin projection is considered to be a separate spin species. Secondly, zero-field splitting results in strongly orientation-dependent effective g factors, which introduce inhomogeneous broadening due to small variations in the orientation of the impurities. This is commonly called g-strain [58,59] and results in underestimated relaxation times.

Subsequently, for a spin S > 1/2 system, the frequency-dependent Bloch susceptibility is extrapolated from the two-state model under the assumption that the 2S spin transitions adhere to the line shape predicted by the derived Bloch susceptibility, i.e.,

$$\chi_{M}^{xy} = \sum_{j=1}^{2S} \frac{\chi_{0,j} \omega_{0,j}}{\omega_{0,j}^{2} - \omega^{2} - 2i\omega/T_{2,j}} \begin{pmatrix} \omega_{0,j} & -i\omega \\ i\omega & \omega_{0,j} \end{pmatrix}, \quad (24)$$

where the superscript xy denotes only the response in the xy plane, or equivalently

$$\chi_{M}^{xy} = \sum_{j=1}^{2S} \frac{\chi_{0,j}\omega_{0,j}}{\omega_{0,j}^{2} - \omega^{2} - 2i\omega/T_{2,j}} \left[\omega \begin{pmatrix} 1 & -i \\ i & 1 \end{pmatrix} + (\omega_{0,j} - \omega) \begin{pmatrix} 1 & 0 \\ 0 & 0 \end{pmatrix} + (\omega_{0,j} - \omega) \begin{pmatrix} 0 & 0 \\ 0 & 1 \end{pmatrix} \right], \quad (25)$$

where $\chi_{0,j}$, $\omega_{0,j}$ and $T_{2,j}$ denote the contribution to the dc magnetic susceptibility, the resonance frequency, and the transverse relaxation time for a given spin projection $j=1,\ldots,2S$, respectively. Here j=1 corresponds to the transition from the lowest to the second lowest-lying state, j=2 from the second to the third lowest-lying state, etc.

E. Bloch eigenmagnetic polarizability model

Inspired by Max Born's description of lattice dynamics in crystalline materials [60], an eigendielectric displacement vector dyad summation was recently proposed as a physical model approach to render the measured dielectric function tensor across the spectral range of j = 1, ..., N long-wavelength active phonon modes [34–38,61]

$$\varepsilon = \varepsilon_{\infty} + \sum_{j=1}^{N} \varrho_{j}(\hat{\mathbf{e}}_{j}^{\dagger} \otimes \hat{\mathbf{e}}_{j}), \tag{26}$$

where ϱ_l is a complex-valued response function representing dispersion and loss caused by phonon mode l, $\hat{\mathbf{e}}_i$ is a vector whose direction renders the maximum response of phonon mode *j* to the electric field component of an electromagnetic wave, † indicates transpose and complex-conjugate, and ⊗ is the dyadic product. $\hat{\mathbf{e}}_i$ further defines a normal to the plane within which the electric field cannot excite mode j. The obvious advantage of this summation approach lies in the possibility to add contributions of individual dipolar linear optical excitations to the total response function of a given material, i.e., the dielectric function tensor. The eigenpolarization direction parameter $\hat{\mathbf{e}}_i$ and eigendielectric function ϱ_i were demonstrated as necessities to correctly describe and determine phonon mode frequency parameters including their amplitudes and broadening information for materials with low-symmetry lattice structures, i.e., monoclinic and triclinic crystal systems [34-38,61]. The approach is generally valid for all symmetries, and correctly predicts generalized, coordinate-invariant representations of the dielectric functions

and coordinate-invariant formulations of the Lyddane-Sachs-Teller relationship [36], the evolution of longitudinal phonon mode coupling with free charge carriers [40], the existence of hyperbolic shear polaritons [62], and the anisotropic properties of band-to-band transitions in low-symmetry solid-state materials [63], for example.

It is of interest here to analyze the Bloch susceptibility model for its representation in terms of an analogous summation and the aim is to identify a concept analogous to the summation of lattice excitations, where the occurrence of multiple magnetic excitations can be added arbitrarily with respect to their magnetic polarization properties. The question that follows is, can a similar eigenvector be found which represents a magnetic excitation and a response function be rendered that contains dispersion and loss. Inspecting the result in Eq. (25) one recognizes a dyad decomposition into three contributions such that

$$\mu = 1 + \sum_{j=1}^{2S} \left(\varrho_j^{\text{CP}} (\hat{\mathbf{a}}_j^{\dagger} \otimes \hat{\mathbf{a}}_j) + \varrho_j^{LP} [\hat{\mathbf{x}}_j^{\dagger} \otimes \hat{\mathbf{x}}_j + \hat{\mathbf{y}}_j^{\dagger} \otimes \hat{\mathbf{y}}_j] \right), \tag{27}$$

where $\hat{\mathbf{a}}_j = (1, -i, 0)$, $\hat{\mathbf{x}}_j = (1, 0, 0)$, and $\hat{\mathbf{y}}_j = (0, 1, 0)$. Equation (27) is the Bloch eigenmagnetic polarizability model and is a central finding of this work. We note with interest that dyad $(1, \pm i, 0)^{\dagger}_j \otimes (1, \pm i, 0)$ was shown in Ref. [29] to represent the magnetic susceptibility tensor for a purely left/right-circularly polarized eigenprocess. Eigenvectors $\hat{\mathbf{x}}_j = (1, 0, 0)$ and $\hat{\mathbf{y}}_j = (0, 1, 0)$ are the previously described linear eigenpolarization vectors [34–38,61]. Note that Eq. (27) remains unchanged under rotation around vector $\hat{\mathbf{a}}_j^* \times \hat{\mathbf{a}}_j = (0, 0, -2i)$, where \times indicates the cross or vector product and * is the complex-conjugate. Likewise, rotation around direction $\hat{\mathbf{x}}^* \times \hat{\mathbf{y}} = (0, 0, 1)$ leaves Eq. (27) unchanged. Here, this direction is parallel to the external magnetic field direction, $\frac{\mathbf{B}_0}{B_0}$. Thereby, we can also express the gyration vector of the jth eigenmagnetic polarizability contribution

$$g_j = \frac{i}{2} \hat{\mathbf{a}}_j^{\star} \times \hat{\mathbf{a}}_j = \hat{\mathbf{x}}^{\star} \times \hat{\mathbf{y}}. \tag{28}$$

Note further that rotation of the magnetic susceptibility tensor μ relative to a given sample and ellipsometer coordinate system can be performed simply by using Euler angle rotations and rotation matrix A defined in Appendix B 1. Equation (27) is then rewritten for new $\mu' = A\mu A^{-1}$ by replacing $\hat{\mathbf{e}}_j' = \hat{\mathbf{e}}_j A^{-1}$, $\hat{\mathbf{x}}_j' = \hat{\mathbf{x}}_j A^{-1}$, and $\hat{\mathbf{y}}_j' = \hat{\mathbf{y}}_j A^{-1}$, hence, $g_j' = Ag_j$ [64]. It is commonly assumed that gyration vectors of all j spin resonances are parallel to the external magnetic field, $g_j' = \frac{\mathbf{B}_0}{B_0}$. However, this latter statement may not necessarily be true. Investigations using THz EPR ellipsometry at multiple angles of incidence, for example, could be used to test this assumption in the future.

When the eigenvectors $\hat{\mathbf{a}}_j$, $\hat{\mathbf{x}}_j$, and $\hat{\mathbf{y}}_j$ are all equal among the $j=1,\ldots,2S$ magnetic transitions, then the associated Bloch response function components obtained here are [65]

$$\varrho_{j}^{\text{CP}} = \frac{\chi_{0,j}\omega_{0,j}\omega}{\omega_{0,j}^{2} - \omega^{2} - 2i\omega/T_{2,j}},
\varrho_{j}^{\text{LP}} = \frac{\chi_{0,j}\omega_{0,j}(\omega_{0,j} - \omega)}{\omega_{0,j}^{2} - \omega^{2} - 2i\omega/T_{2,j}},$$
(29)

$$\begin{split} \omega &\to 0 \quad \text{then } \varrho_j^{\text{CP}} \to 0 \\ \omega &\to \omega_{0,j} \quad \text{then } \varrho_j^{\text{CP}} \to 2i\chi_{0,j}\omega_{0,j}T_2 \\ \omega &\to \infty \quad \text{then } \varrho_j^{\text{CP}} \to 0 \\ \omega &\to 0 \quad \text{then } \varrho_j^{LP} \to \chi_{0,j} \\ \omega &\to \omega_{0,j} \quad \text{then } \varrho_j^{LP} \to 0 \\ \omega &\to \infty \quad \text{then } \varrho_j^{LP} \to 0. \end{split}$$

The two functions differ subtly in their spectral dependencies. The circularly polarized process is linear in the external magnetic induction, B_0 , while the linearly polarized process has a component which is linear and another which is quadratic in B_0 . The circularly polarized process disappears when ω approaches zero and infinity, while at resonance, the response function is purely imaginary and the amplitude is proportional to the magnetization associated with the l^{th} spin transition, its frequency, and transverse relaxation time. At resonance, there is no linearly polarized component of the magnetization. The latter also vanishes at infinite frequencies. However, at zero frequency, the linear polarizability function reveals $\chi_{0,j}$. The linear components constitute a superposition of two equivalent linear eigenmagnetic contributions polarized within the (x, y) plane in this coordinate system and the response within this plane is isotropic.

It is useful to introduce the Bloch susceptibility function for magnetic transition j, $\chi_{Bl,j}$

$$\chi_{\mathrm{Bl},j} = \frac{\chi_{0,j}\omega_{0,j}\omega}{\omega_{0,j}^2 - \omega^2 - 2i\omega/T_{2,j}};\tag{31}$$

and rewrite Eq. (29)

$$\varrho_l^{\text{CP}} = \chi_{\text{BI},j};$$

$$\varrho_l^{\text{LP}} = \chi_{\text{BI},j} \frac{\omega_{0,j} - \omega}{\omega}.$$
(32)

We can then express, and plot if necessary, the scalar, complex-valued Bloch permeability eigenfunction as a sum over all Bloch susceptibility functions for all magnetic transitions j = 1, ..., 2S

$$\mu_{\rm Bl} = 1 + \sum_{i,1}^{2S} \chi_{{\rm Bl},j}.$$
 (33)

We propose use of Eq. (27) and its component vectors and functions as suitable decomposition approach to analyze the measured spectral appearances of real and imaginary parts of the permeability function, for example, obtained from THz-EPR ellipsometry, or magnetooptic ellipsometry investigations. We note that Eq. (27) is applicable for all magnetic field orientations, necessitating only an appropriate rotation of the tensor to ensure consistency in the analysis of the ellipsometry data. As such, this is a new approach for the study of the polarization response of spin transitions affected by zero-field splitting. We also propose use of Eq. (33) to present and discuss the spectral response of spin transitions if such can be considered to share a common gyration vector. Future work will illuminate properties and usefulness of this approach.

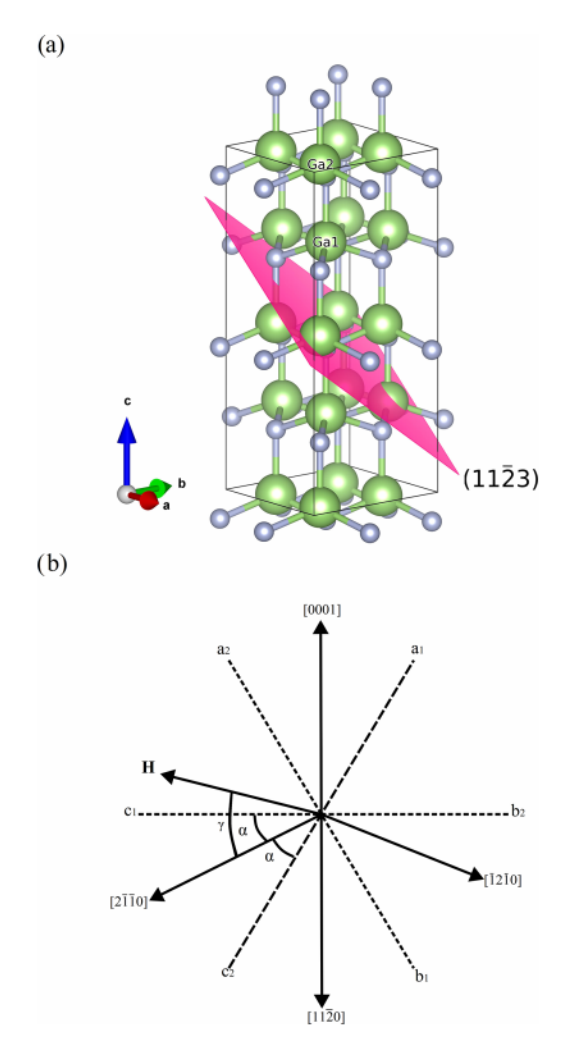


FIG. 1. (a) Wurtzite crystal structure of GaN along the $[000\bar{1}]$ direction (c axis). The nitrogen atoms are depicted in blue color and the gallium atoms are depicted in green color and denoted by either Ga1 or Ga2, depending on the relative rotation of the two nonequivalent gallium sites with respect to the internal ligand field. The GaN (11 $\bar{2}$ 3) plane is shown. Produced with computer software VESTA [70]. (b) Orthographic projection (the axes are pointing out-of-plane) of selected crystallographic and ligand-field axes (a_1, b_1, c_1) and (a_2, b_2, c_2) of the two gallium sites onto the (11 $\bar{2}$ 3) plane. This figure schematically illustrates the definitions of the angles α and γ , along with an arbitrarily oriented magnetic field. For more details on the coordinate system of the spin Hamiltonian, we refer to Ref. [69], from which this figure is adapted.

F. Hamiltonian of the S = 5/2 Fe3+ impurity in GaN

Iron-doped wurtzite GaN has previously been studied extensively by several groups [51,66,67], where it was observed that iron takes on the Fe³⁺ charge state that has a total spin S=5/2 and orbital angular momentum L=0. The ground state is thus ${}^6S_{5/2}$. Furthermore, in GaN, there are two Ga sites that are inequivalent with regard to the internal crystal field due to the neighboring N and Ga ions as illustrated in Fig. 1. It is possible to direct the external magnetic field in such a way that the two inequivalent sites are rendered equivalent, and in that case, yield the energy-level diagram shown in Fig. 2, where the magnetic field is assumed to be 45° towards

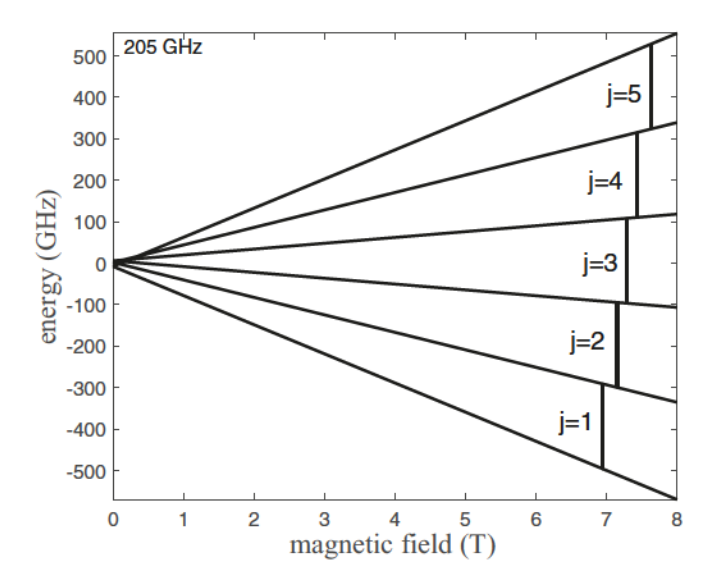


FIG. 2. Energy-level diagram for the two inequivalent sites of the Fe³⁺ impurity in GaN, with the magnetic field directed 45 degrees towards the crystallographic c axis with the sample in-plane direction such that the two inequivalent Ga sites are equivalent with regards to the internal crystal field. The allowed $\Delta m_s = \pm 1$ transitions at 205 GHz are indicated by vertical black lines, with corresponding numbers to identify each transition. Simulated using the software package EASYSPIN [58].

the crystallographic c axis. Moreover, it was shown that the spin-Hamiltonian suggested by Bleany $et\ al.$ [68] and altered by Geschwind [69] suffices to explain the experimental results and local symmetry of the $S=5/2\ {\rm Fe}^{3+}$ impurity

$$\mathcal{H} = g\mu_B B_0 \mathbf{S}_z \cos\theta + \frac{1}{2} g\mu_B B_0 \sin\theta (\mathbf{S}_+ + \mathbf{S}_-)$$

$$+ D \left(\mathbf{S}_z^2 - \frac{1}{3} \mathbf{S} (\mathbf{S} + 1) \right) - \frac{1}{180} (a - F)$$

$$\times \left(35 \mathbf{S}_z^4 - 30 \mathbf{S} (\mathbf{S} + 1) \mathbf{S}_z^2 + 25 \mathbf{S}_z^2 - 6 \mathbf{S} (\mathbf{S} + 1) + 3 \mathbf{S}^2 (\mathbf{S} + 1)^2 \right)$$

$$\times \frac{\sqrt{2}}{36} a (\mathbf{S}_z (\mathbf{S}_+^3 e^{-i3(\psi \pm \alpha)} + \mathbf{S}_-^3 e^{i3(\psi \pm \alpha)})$$

$$+ (\mathbf{S}_\perp^3 e^{-i3(\psi \pm \alpha)} + \mathbf{S}_-^3 e^{i3(\psi \pm \alpha)}) \mathbf{S}_z). \tag{34}$$

Here, the g factor is taken to be isotropic, and S, S_+ , S_- and S_z are the usual S = 5/2 spin matrices. Furthermore, the effect of zero-field splitting is represented in Eq. (34) by D and F, which are the axial crystal field parameters to the second and fourth order, respectively, and a is the cubic crystal field parameter. Kashiwagi et al. [51] conclusively demonstrated by applying Eq. (34) to conventional X- and Q-band EPR that Fe³⁺ substitution of Ga³⁺ in GaN occurs, and observed that there are two nonequivalent Ga sites in wurtzite GaN with respect to the internal crystal field (Fig. 1). The nonequivalence is due to the two sites' different rotations with regard to the internal crystal (ligand) field, and thus have different α angles, as discussed below. In addition, the selection rule $\Delta m_s = \pm 1$, where m_s is the sextet of projections, suggests that five spin transitions are allowed for each of the two sites, resulting in up to a total of ten allowed spin transitions. The angles

 θ , γ , and α correspond to the angle between the magnetic field and the [0001] axis, the angle between the magnetic field projection onto (11 $\bar{2}$ 3) and the [10 $\bar{1}$ 0] direction, and the angle between the cubic crystal field axis $a_{1,2}$ and the [2 $\bar{1}\bar{1}$ 0] direction, respectively, are depicted in Fig. 1. For all measurements, the sample was rotated such that it rendered the two distinct sites equivalent in terms of the crystal field, consequently resulting in a total of five discreet spin transitions observable within each spectrum. This is the case when the magnetic field is aligned with $\langle 1\bar{1}00\rangle$. Consequently, the spin species corresponding to each of the two sites are treated as one, which is an exception for this given rotation.

G. Brillouin magnetization of the S = 5/2Fe3+ impurity in GaN

In extension to using Eq. (20) and to best-match model the frequency-dependent permeability function we augment additional constraints for our specific S = 5/2 system. The constraints affect the amplitude values of the spin transitions at a fixed magnetic field, and are obtained from the summation of magnetic moments according to their thermal population. This constraint then permits the use of the spin volume concentration n_s as the input parameter for the MMF approach. A similar analysis was performed by Maryasov and Bowman on a S = 5/2 system [71]. We start by writing the dc magnetization as

$$M_0 = -\frac{g\mu_B}{2}((n_{+1/2} - n_{-1/2}) + 3(n_{+3/2} - n_{-3/2}) + 5(n_{+5/2} - n_{-5/2})).$$
(35)

The expression, sometimes referred to as Brillouin magnetization, can be comprehended as an outcome wherein each unpaired electron contributes $gm_s\mu_{\rm Bl}$ to the overall magnetization, and $n_{+1/2}, n_{-1/2}$, etc., refer to the spin population volume density in level +1/2, -1/2, etc. Furthermore, Eq. (35) can be restructured as

$$M_0 = \frac{g\mu_B}{2} (5(n_{+3/2} - n_{+5/2}) + 8(n_{+1/2} - n_{+3/2}) + 9(n_{-1/2} - n_{+1/2}) + 8(n_{-3/2} - n_{-1/2}) + 5(n_{-5/2} - n_{-3/2})) = \sum_{i}^{5} M_{0,i},$$
(36)

i.e., as a sum corresponding to the five allowed spin transitions. The occupancy of each state is given by its Boltzmann factor

$$n_{n-1} - n_n = \frac{e^{-E_{n-1}/kT} - e^{-E_n/kT}}{\sum_{s} e^{-E_{s}/kT}} n_s,$$
 (37)

where the energy levels E_n are given by the eigenvalues of Eq. (34), and n_s is the spin volume concentration that is assumed to be equivalent to the concentration of iron impurities situated on any of the two gallium sites. In the same manner, the dc magnetic susceptibility function is modeled as a sum of all allowed spin transitions contributing independently

$$\chi_0 = \frac{M_0}{B_0} = \sum_{j}^{5} \frac{M_{0,j}}{B_0} = \sum_{j}^{5} \chi_{0,j}.$$
 (38)

Hence, Eq. (37) provides specific ratios between amplitude strengths among the five transitions of the S = 5/2 spin sys-

tem for any given magnetic field B_0 , and the scaling factor on all amplitudes provides the spin density, which is analogus to the impurity concentration for a given site. Because the magnetic field changes the eigenenergies, the ratios of amplitudes change as well, which can be measured by THz-EPR ellipsometry. Hence, measurements at different magnetic fields and/or different temperatures combined provide sensitivity to the spin density.

III. EXPERIMENTS AND METHODS

A. Sample

We conduct a quantitative assessment of the THz permeability properties of a wurtzite-structure single crystalline GaN bulk sample doped with iron. The GaN sample with (0001) c-plane surface orientation is fabricated by hydride vapor phase epitaxy [72]. The sample thickness of 0.365 mm, as measured by THz ellipsometry, agrees very well with the value of 0.350 ± 0.015 mm, specified by the provider Suzhou Nanowin Science and Technology Co. Ltd. The lateral dimensions of the GaN sample are 20×20 mm². The dislocation density in the GaN samples was estimated from x-ray diffraction [73] and cathodoluminescence panchromatic imaging [74] to be in the order of 1×10^7 cm⁻². The GaN sample is semi-insulating with a resistivity $>10^6$ Ω cm at 300 K.

B. THz-EPR ellipsometry

Measurements of the Mueller matrix elements are performed using an in-house built THz ellipsometer system at the Terahertz Materials Analysis Center at Lund University. The instrument uses a dual-rotating waveplate setup with fast continuing frequency-sweeping, which differs from the optical Hall effect and THz EPR generalized ellipsometry instruments described in our previous works [26–29]. Note that the instrument incorporates additional anisotropic polarizing optical elements allowing for the measurements of the 15 normalized Mueller matrix elements as reported here. It further uses a fixed linear polarizer, rotating waveplate, sample, rotating waveplate, and fixed linear polarizer (analyzer) configuration. The instrument calibration and operation schemes for data acquisition follow the same procedures described by Ruder et al. [75,76]. The anisotropic waveplates consist here of 3D-printed plastic slanted columnar thin films. Such structures produce sufficient anisotropy in the THz spectral range to modulate the Stokes vector components at normal incidence transmission upon rotating the waveplates around its surface normal [77,78]. A more detailed instrument description will be provided elsewhere. For measurements with the sample immersed in a magnetic field, a superconducting split-coil magnet is employed, capable of creating magnetic fields from -8 to 8 T with a magnetic field homogeneity of approximately 3000 ppm across a central cylindric volume with a diameter of 10 mm (Cryogenics Ltd. London UK). Further details of the magnet setup are given in Refs. [27,29].

THz EPR ellipsometry measurements were performed in the spectral range from 199–208 GHz in steps of 9.8 MHz. The source bandwidth was approximately 50 kHz. The instrument uses a solid-state synthesizer source with digital control over frequency and duty cycle [29]. The Mueller matrix elements are obtained from a subsequent collection of intensity readings at the solid-state detector for various settings of polarizer, waveplate 1, waveplate 2, and analyzer as described by Ruder et al. [75,76]. Although the waveplates are not ideal, they still provide enough modulation to determine the handedness of the elliptically polarized light, which is sufficient to resolve the full Mueller matrix. The instrument then records the full 4×4 Mueller matrix, i.e., 16 elements normalized by element M_{11} . Measurements are performed in reflection configuration with the sample positioned between the split coils at 45° angle of incidence. In this configuration, the magnetic field direction aligns parallel with the incident beam. Thereby the magnetic field is oriented at an angle of 45° towards the crystallographic axis c of the GaN sample. Additionally, the sample is rotated around its normal (azimuthal rotation) to achieve positioning of the two nonequivalent gallium sites with respect to the static magnetic field such that their respective magnetic spin eigenenergy values coincide. This is the case when the projection of the magnetic field in the sample plane is aligned with [1100] or an equivalent direction as described in Sec. IIF. As a result, the two quintuplets merge and appear exactly one quintuplet in the THz-EPR ellipsometry spectra. This orientation is selected here for the purpose of simplifying the analysis by reducing necessary model calculations because the thermodynamic distribution across one common spin system must be considered only. The purpose of the experiment is to demonstrate the approach. The sample temperature is held constant during measurements. Data were measured at temperatures of 20 and 30 K, and at a magnetic field strength of -7.23 and 7.23 T. Data were also measured at zero magnetic field, and the zero-magnetic field data were subtracted from the magnetic field data in order to determine small-signal difference data which were then used as target data during the subsequent Hamiltonian and best-match model calculation analyses. Finally, the data collected from the -7.23 T scan were subtracted from the +7.23 T scan, to further amplify the signal strength.

C. Ellipsometry model calculations

The ellipsometry data model analysis is performed using the Berreman [79] 4 × 4 transfer matrix approach augmented with modifications described by Schubert [80]. The approach is briefly summarized in Appendix A. A three-phase Al holder-GaN sample-air model is used. The Al holder reflects 100% of the incident electromagnetic waves and it is modeled as a highly conductive material using the isotropic Drude model, $\varepsilon = 1 - \frac{\omega_p^2}{\omega(\omega - i\gamma_p)}$ with plasma frequency $\omega_p = 10^{-6}$ cm⁻¹ and plasma scattering time $\gamma_p = 0$ cm⁻¹. The dielectric properties of the GaN sample were calculated using the anisotropic dc dielectric constant values reported by Hibberd *et al.* [81], where ε_a and ε_c refer to the dielectric permittivity for polarization along crystal axes a and c, respectively,

$$\epsilon = \begin{pmatrix} \varepsilon_a & 0 & 0 \\ 0 & \varepsilon_a & 0 \\ 0 & 0 & \varepsilon_c \end{pmatrix} = \begin{pmatrix} 9.22 & 0 & 0 \\ 0 & 9.22 & 0 \\ 0 & 0 & 10.32 \end{pmatrix}, \quad (39)$$

and wherein the coordinate system (x', y', z') of the dielectric tensor is congruent with the laboratory reference frame utilized for the ellipsometric data evaluation. Note that due to the fact that Fe acts as compensating dopant in GaN, the material is electrically fully insulating and no Drude model contribution to the model dielectric tensor is necessary. The permeability tensor was modeled according to Eq. (20) and the parameters were inferred from the best-match parameter model described below. This tensor undergoes a rotation, explained in Appendix B 1, employing Euler angles $\psi = -90^{\circ}$ and $\theta = 45^{\circ}$. This rotation is imperative to align the tensor's gyration [Eq. (28) in Sec. II E] axis with the externally applied magnetic field and to align the (x, z) plane with the incidence plane of the electromagnetic wave. Subsequently, both the dielectric and permeability tensors are integrated into the $\hat{\Delta}$ matrix (Appendix A). This integration facilitates the computation of the optical response via the 4×4 -matrix approach.

From the 4×4 -matrix method, the calculated Mueller-matrix elements M_{23} , M_{32} , M_{14} and M_{41} are compared to the best-match model. These specific elements are most sensitive to spin transitions and are thus chosen. A more detailed explanation of how these are calculated is presented in Appendix B. To improve the signal-to-noise ratio, we add M_{32} to M_{23} and subtract M_{41} from M_{14} , because from the permeability tensor model (20) used in our analysis it follows that $M_{32} = M_{23}$ and $M_{14} = -M_{41}$. This can be seen directly in the full Mueller matrix element spectra set in Fig. 4. As such, "effective" Mueller-matrix elements are calculated from experimental and model calculated data

$$M_{23+32} = \frac{M_{23} + M_{32}}{2} \tag{40}$$

and

$$M_{14-41} = \frac{M_{14} - M_{41}}{2}. (41)$$

D. MMF parameter regression analysis

The best-match model was calculated using the *curve_fit* function from the SCIPY library [82]. The *curve_fit* function uses a trust region reflective algorithm, which aims to minimize the sum of squared residuals

$$S = \sum_{i=1}^{j} (y_i - f_i)^2, \tag{42}$$

where the sum runs over all frequencies, $y_i = [M_{23+32}, M_{14-41}](\omega_i)$ at frequency ω_i , and N is the total number of frequencies at which Mueller matrix elements were included into the regression analysis. The model response f_i is calculated by simultaneously optimizing parameters related to the spin-Hamiltonian D, a, F, g, and θ , and the Bloch permeability parameters n_s and $T_{2,j}$ for all $j=1,\ldots,5$ spin transitions. Error estimates are determined as the square root of the diagonal elements of the covariance matrix, as computed by the curve-fitting procedure. Note that no data-point uncertainty-based biasing was performed in Eq. (42) because the experimentally determined uncertainty (variance) on every Mueller matrix element was observed to

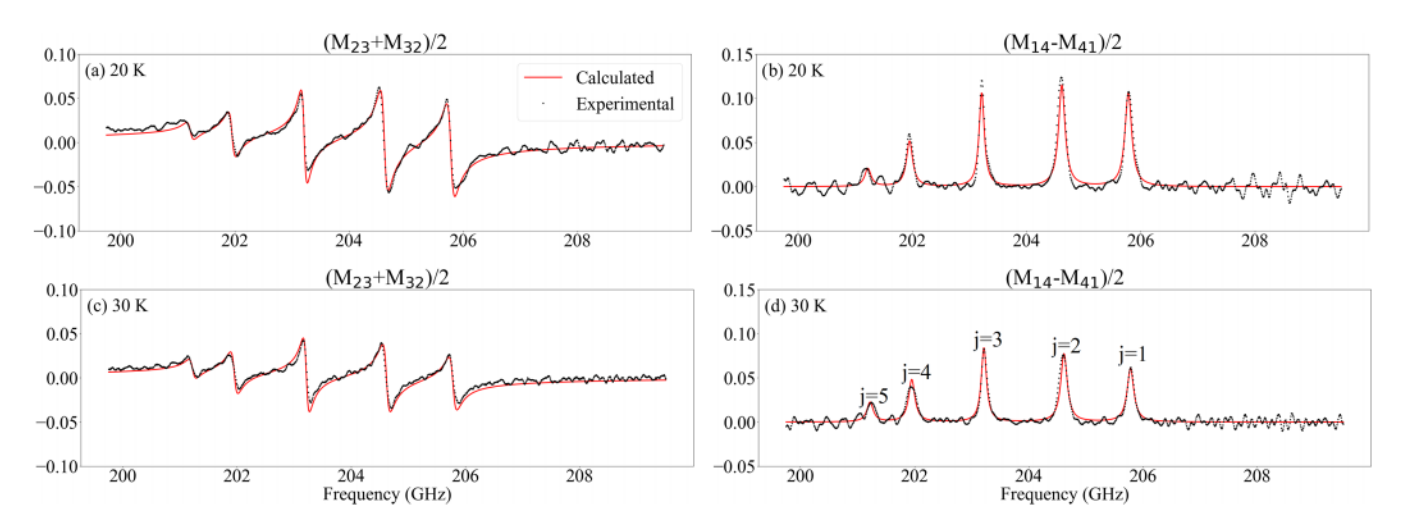


FIG. 3. Results from frequency-swept THz-EPR ellipsometry measurements performed at [(a) and (b)] 20 K and [(c) and (d)] 30 K. The calculated best-match model is represented by the solid red line and is based on the Bloch-Brillouin model. The black symbols indicate the experimental data. In (a) and (c), $M_{23+32} = (M_{23} + M_{32})/2$ is shown, which scales with circular birefringence. In (b) and (d), $M_{14-41} = (M_{14} - M_{41})/2$ is shown, which scales with circular dichroism. Experimental and model data are obtained as difference data for magnetic field B = -7.23 and 7.23 T. In (d), the corresponding index for each transition is indicated.

be uniform (\approx 0.01%, see Fig. 4) across the spectral range investigated.

IV. EXAMPLE: SPIN TRANSITIONS IN FE-DOPED GAN

The experiment on the spin S = 5/2 system in GaN is selected here for the purpose of demonstration. THz EPR ellipsometry was performed as described above. The Hamiltonian description of the zero-field split system is well known, and thereby is suitable for the purpose here. As outlined in earlier sections, the sample is oriented such that the two zero-field splitting quintuplets align in their eigenvalues and thermodynamic spin distributions. As a result, only one common quintuplet is observed.

A. Results

Figures 3(a)-3(d) show experimental and best-match model calculated data for M_{14-41} and M_{23+32} at 20 and at 30 K, respectively. Note the different amplitude distributions between the different temperature measurements. The full sets of Mueller matrix data taken at the two magnetic fields at 20 K are shown in Fig. 4. The best-match model calculated data are obtained by varying the Hamiltonian parameters for calculation of the eigenenergies $\omega_{0,j}$, the total spin density and impurity concentration n_s , and the transverse relaxation time parameters for each transition. An excellent match between experimental and model-calculated data is obtained. The match supports the validity of the model derived in this work. Particularly, the match upon reversal of magnetic field, which changes signatures such that $M_{14}(B) = M_{41}(-B), M_{23}(B) =$ $-M_{32}(-B)$ as well as $M_{14}(B) = -M_{41}(B)$ and $M_{23}(B) =$ $M_{32}(B)$, as can be seen in Fig. 4 is consistent between experiment and theory. This observation is the first to our knowledge because no Mueller matrix elements have been reported thus far for spin resonances in the THz spectral range. Equation (20) can account for the expected sign change upon magnetic field reversal experimentally observed here, which

was not the case with the *ad hoc* model used previously for THz-EPR ellipsometry data analysis [29]. There, the permeability tensor suffered from being invariant to a change of the sign of ω_0 .

The congruence between the model and experimental observations is further noteworthy because the amplitude variations are consistent with predictions derived from the Brillouin magnetization theory, with the only model parameters used to calculate ten amplitudes over the two measurements being the spin volume concentration and the zero-field splitting parameters. Moreover, the spectral line shapes align with the theoretical projections based on the Bloch equations. This can be seen by the amplitude distribution match in Figs. 3(a)-3(d) as well as in the full Mueller matrix displayed in Fig. 4. The extracted Bloch permeability $\mu_{\rm Bl}$ as given by Eq. (33) obtained from the experimental data at 7.23 T and 20 K is shown in Fig. 5. This result highlights the ability of the method to measure and determine both the imaginary and real parts of the frequency-dependent permeability tensor and thus yield access to further polarization properties of a given magnetic transition as well as the possibility of inferring dc properties by extrapolating the value of μ_{Bl} at $\omega = 0$.

The zero-field splitting, *g* factor, and spin density parameters deduced from our best-match model calculations are cataloged in Table I. The transverse relaxation times are summarized in Table II.

B. Discussion

The zero-field splitting parameters deduced here agree well with those reported in prior studies [51,66,67]. Nevertheless, the substantial standard deviations, in particular for parameters a and F indicate that multiple combinations of the zero-field splitting parameters can produce equally satisfactory model calculations matching our data obtained for a singular sample azimuth (rotation) orientation. Additionally, a small angular offset between the magnetic field direction

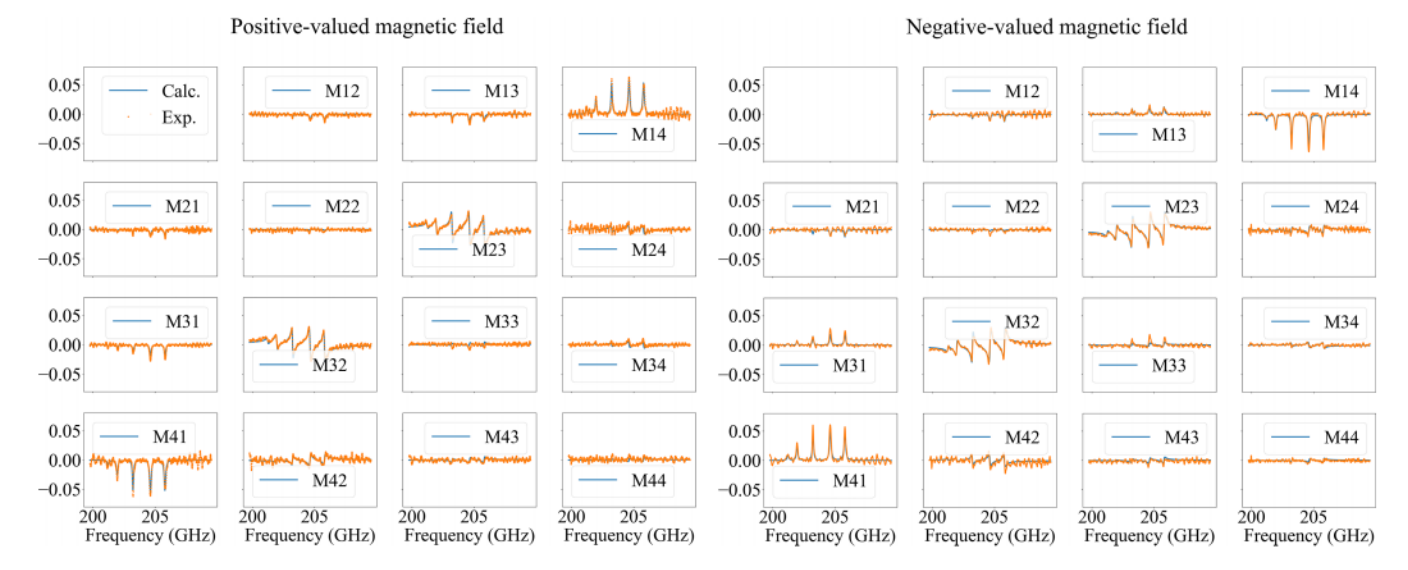


FIG. 4. Orange dots represent experimental data collected from terahertz magnetic resonance ellipsometry at 20 K, showing the difference between measurements at 0 and 7.23 T on the left side, and 0 and -7.23 T on the right side. The blue solid line indicates the calculated best-fit model based on the Bloch model described in the text.

and the sample plane was observed and is due to a slight misalignment of the magnet cryostat to dampen standing waves within the inner wedged diamond windows of the cryostat. The quantitatively determined spin volume concentration n_s is in agreement with the nominal range of iron concentration of this specific sample. In light of these findings, a future comprehensive analytical investigation is warranted to ascertain the reliability and accuracy of this technique for measuring spin volume concentration by augmenting further magnetic field, temperature, and sample rotation data.

The calculated transverse relaxation times are presented in Table II. It is important to emphasize that these relaxation times are inflated due to the rather large magnetic field broadening introduced by our superconducting magnet, which is not engineered for optimal magnetic field homo-

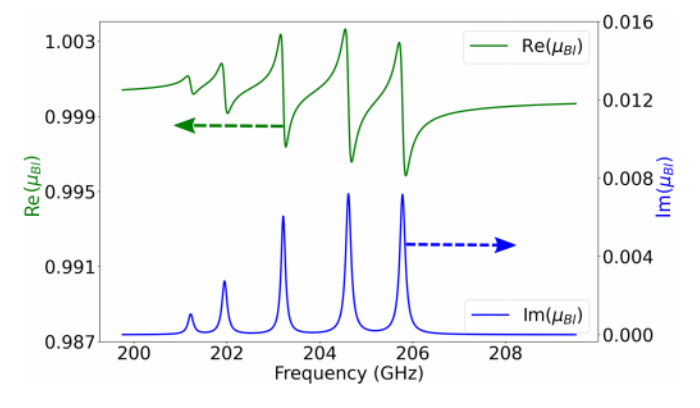


FIG. 5. Extracted Bloch permeability eigenfunction μ_{Bl} at B=7.23 T and 20 K from the best-match model according to (33). The lower part shows the imaginary part of μ_{Bl} as a solid blue line, and the upper half shows the real part of μ_{Bl} as a solid green line. The distribution of amplitudes across the five spin transitions is the result of the thermodynamic Brillouin model, the eigenfrequencies are the result of the Hamiltonian calculations predicting the zero-field splitting spin transition in this example.

geneity. This lack of flatness introduces a notable broadening of the observed transitions [83]. To obtain more accurate relaxation time parameters, a thorough consideration of the broadening causes attributable to both the magnetic field inhomogeneity and g-strain is required. However, such an in-depth analysis falls beyond the scope of this article. It is noted that the $T_{2,j}$ values differ among the transitions. The cause of this could be due to several reasons, such as the two nonequivalent sites not perfectly overlapping or the width of the transitions being unequal because of the difference in how the spin projections interact with the local environment. The longitudinal relaxation times are not accessible from this steady-state continuous-wave single-frequency type measurement, and time-dependent measurement approaches are necessary. Such are conceivable using solid-state source- and detector-based techniques and could be the subject of further investigations. We propose that THz-EPR ellipsometry is a robust technique for investigating transverse spin relaxation times, offering significant potential for future studies in this domain.

The pairs of Mueller matrix elements M_{14} , M_{41} and M_{23} , M_{32} are routinely associated with circular dichroism and circular birefringence. [84] Hence, one can interpret data in Figs. 3(a) and 3(b) with circular dichroism and in Figs. 3(c) and 3(d) with circular birefringence. The former is then expected to appear as a Lorentzian absorption line, while the latter is expected to appear as a form with increasing normal dispersion towards resonance, negative dispersion across resonance, and normal dispersion approaching zero above resonance. Note that all features shown in Figs. 3(a)-3(d) invert with magnetic field reversal, while spectra shown in Fig. 5 remain unchanged. This is due to the definition we chose in Sec. II E. Then, function μ_{Bl} represents the LCP circular birefringence in its real part and circular polarized loss in its imaginary part for positive magnetic field. Upon magnetic field reversal, μ_{Bl} then represents the RCP circular birefringence in its real part and circular polarized loss in its imaginary part. Both functions are unchanged between

TABLE I. Summary of model parameters obtained from analysis of the THz-EPR ellipsometry measurements on iron-doped GaN. The parameters were determined by minimizing the least-squares difference between the best-match model and experimental data gathered at temperatures of 20 and 30 K. The optimization process was confined to the Mueller-matrix elements M_{23} , M_{32} , M_{14} , and M_{41} . All parameters are shown with error bars according to one standard deviation as approximated from the square roots of the covariance matrix.

	D MHz	a MHz	F MHz	g n/a	$ heta^\circ$	$n_s \mathrm{cm}^{-3}$
This work	-2250 ± 14	210 ± 280	15 ± 280	$2.008200 \pm 8 \times 10^{-6}$	44.4 ± 0.05	$1.92 \times 10^{18} \pm 1.57 \times 10^{16}$
Kashiwagi et al.a	-2290	240	-27	2.008	_	_
Maier et al.b	-2138	144	-12	1.995	_	_
Baranov et al.c	2144	_	_	1.994	_	_

aX- and Q-band EPR, Ref. [51].

LCP at positive and RCP at negative magnetic fields. Hence, $\mu_{\rm Bl}$ directly represents the chiroptical properties of magnetic resonance transitions. We note that signatures observed in our experiment relate to electron spin resonance.

Future research trajectories may consider the implementation of advanced versions of the Bloch equations to delve deeper into magnetic resonance phenomena. This includes the Bloch-Bloembergen equations [85] which modify the external magnetic field to an effective magnetic field that encompasses the internal magnetic field generated by the sample, thereby making it more suitable for systems with higher spin volume concentrations. This modification allows for a more accurate representation in ferromagnetic resonance studies. In parallel, both the Gilbert equation [86] and Landau-Lifshitz equation [87] offer a reformulation where phenomenological relaxation times are substituted with a relaxation rate that is proportional to the time derivative of the magnetization, accompanied by a damping parameter. This damping parameter is crucial in the study of energy dissipation within the system, particularly relevant for the investigation of spin waves and strong ferromagnets characterized by interacting magnetic moments and domain formation [88]. The Bloch-McConnell [42] equations represent another extension of the original Bloch equations, designed to include the dynamics of chemical exchange processes in NMR studies. These modified equations are essential for examining the interaction of nuclear spins in systems where species undergo interconversion, leading to distinct NMR signatures. By integrating terms for chemical exchange rates, the Bloch-McConnell equations enhance the capability to analyze the impact of such exchanges on the system's magnetization. The Bloch equations can also be applied to pulsed magnetic resonance [89], making it feasible to study fast processes such as spin dynamics in biological samples [90].

TABLE II. Measured transverse relaxation time $T_{2,j}$ parameters and one standard deviation in units of 10^{-11} s for various temperatures.

T K	$T_{2,1}$ 10^{-11} s	$T_{2,2}$ 10^{-11} s	$T_{2,3}$ 10^{-11} s	$T_{2,4}$ 10^{-11} s	$T_{2,5}$ 10^{-11} s
20	224 ± 5	232 ± 5	288 ± 7 260 ± 5	240 ± 10	238 ± 24
30	215 ± 5	217 ± 4		191 ± 6	223 ± 13

V. CONCLUSIONS

We presented a generalized approach based on Bloch's equation of motion of nuclear magnetic moments. Our approach can model the frequency, magnetic field, moment density, and temperature dependencies of the permeability in magnetic resonance. Our model predicts polarization properties in electromagnetic wave interactions, which can be observed, for example, in full polarization-resolved Mueller matrix element spectra measured across magnetic resonances as a function of frequency, magnetic field, spin density, and temperature. Thermodynamic considerations are augmented using the concept of Brillouin magnetization. Hamiltonian perturbation approaches for zero-field splitting and Zeeman interaction are incorporated further and the magnetic eigenvalue spectrum, spectral amplitude distribution, and geometrical orientation parameters of the magnetic moment density are obtainable from comparing the generalized model approach to experimental data. We demonstrate the validity of our approach by analyzing the oblique angle of incidence terahertz spectral range magnetic field ellipsometry to detect electron spin resonance quintuplet transitions in wurtzitestructure GaN doped with iron. Measurements at magnetic fields of ± 7.23 T and cryogenic temperatures of 20 and 30 K detail the occurrence of linear and circular birefringence and dichroism associated with each of the zero-field split spin transitions in the S = 5/2 system. We derive and discuss the spectral dependence of the magnetic susceptibility function and obtain the temperature and magnetic field-dependent Hamiltonian parameters and spin density. The 15 independent elements of the normalized Mueller matrix for both positive and negative magnetic fields are matched excellently with our model. We propose the employment of our approach to study magnetic resonance in ferromagnetic, antiferromagnetic, and nuclear magnetic resonance spectroscopy.

ACKNOWLEDGMENTS

This work is supported by the Swedish Research Council under Grants No. 2016-00889 and No. 2022-04812, by the Knut and Alice Wallenberg Foundation funded grant "Wide-bandgap semiconductors for next generation quantum components" (Grant No. 2018.0071), by the Swedish Foundation for Strategic Research under Grant No. EM16-0024, by the Swedish Governmental Agency for Innovation Systems VINNOVA under the Competence Center Program

^bReference [67].

^cX-band EPR, Ref. [66].

Grant No. 2022-03139, and by the Swedish Government Strategic Research Area NanoLund and in Materials Science on Functional Materials at Linköping University, Faculty Grant SFO Mat LiU No. 009-00971. M.S. acknowledges support by the National Science Foundation under awards ECCS 2329940, and OIA-2044049 Emergent Quantum Materials and Technologies (EQUATE), by Air Force Office of Scientific Research under awards FA9550-19-S-0003, FA9550-21-1-0259, and FA9550-23-1-0574 DEF, and by the University of Nebraska Foundation. M.S. also acknowledge support from the J. A. Woollam Foundation.

APPENDIX A: 4 x 4 MATRIX FORMALISM

To compute the Mueller matrix and establish a connection between experimental data and a theoretical model, employing the 4×4 formalism introduced by Berreman [79] is convenient. This formalism was further elaborated upon by Schubert [80]. Fundamentally, the formalism is based on the transfer matrix equation, which can be written as within the coordinate system introduced in Ref. [80]

$$\begin{pmatrix} E_p^I \\ E_s^I \\ E_p^R \\ E_s^R \end{pmatrix} = \mathbf{L} \begin{pmatrix} E_p^T \\ E_s^T \\ E_p^B \\ E_s^B \end{pmatrix}, \tag{A1}$$

$$\hat{\Delta} = \begin{pmatrix} -q_x \frac{\varepsilon_{xx}}{\varepsilon_{zz}} & q_x \Big(-\frac{\varepsilon_{zy}}{\varepsilon_{zz}} + \frac{\mu_{zz}}{\mu_{zz}} \Big) & \mu_{yx} - \frac{\mu_{yz}\mu_{zx}}{\mu_{zz}} & -q_x^2 \frac{1}{\varepsilon_{zz}} + \mu_{yy} - \frac{\mu_{yz}\mu_{zy}}{\mu_{zz}} \\ 0 & -q_x \frac{\mu_{xz}}{\mu_{zz}} & -\mu_{xx} + \frac{\mu_{zz}\mu_{zx}}{\mu_{zz}} & -\mu_{xy} + \frac{\mu_{zz}\mu_{zy}}{\mu_{zz}} \\ -\varepsilon_{yx} + \frac{\varepsilon_{yz}\varepsilon_{zx}}{\varepsilon_{zz}} & -\varepsilon_{yy} + \frac{\varepsilon_{yz}\varepsilon_{zy}}{\varepsilon_{zz}} + q_x^2 \frac{1}{\mu_{zz}} & -q_x \frac{\mu_{zz}}{\mu_{zz}} & q_x \Big(\frac{\varepsilon_{yz}}{\varepsilon_{zz}} - \frac{\mu_{zy}}{\mu_{zz}} \Big) \\ \varepsilon_{xx} - \frac{\varepsilon_{xz}\varepsilon_{zz}}{\varepsilon_{zz}} & \varepsilon_{xy} - \frac{\varepsilon_{xz}\varepsilon_{zy}}{\varepsilon_{zz}} & 0 & -q_x \frac{\varepsilon_{zz}}{\varepsilon_{zz}} \end{pmatrix},$$

where $q_x = n_I \sin\theta$ is the x component of the reduced wave vector $\frac{\omega}{c}\mathbf{q} = \mathbf{k}$ of the incoming wave vector \mathbf{k} at the sample surface parallel to the plane of incidence, n_I is the index of refraction of the isotropic incident medium, and θ is the angle of incidence to the surface normal. In this coordinate choice, the plane of incidence is the (x, z) plane, the sample surface is parallel to the (x, y) plane, z points into the sample, and the surface is at the coordinate origin of the Cartesian system (x, y, z). Given that spin transitions manifest as magnetic resonances, it becomes imperative to model the permeability tensor in addition to the permittivity tensor.

APPENDIX B: MUELLER MATRIX ELEMENTS

Once the transfer matrix is calculated, determining the Mueller matrix elements becomes a straightforward task. For an in-depth explanation, readers are referred to Refs. [33,48,50,91]. To exemplify the procedure, the derivation of elements $M_{14,41}$ and $M_{23,32}$ from the result of the 4 × 4 calculation scheme are presented here. It has been observed that the Mueller-matrix elements $M_{14,41}$ are proportional to the circular dichroism, and the Mueller-matrix elements

where I and R pertain to the electric components of the incoming and reflected electromagnetic (EM) waves, while B and T correspond to the electric components of the backwardtraveling and transmitted portions of the outgoing EM waves. The transfer matrix L consists of three factors:

$$\mathbf{L} = \mathbf{L}_I^{-1} \prod_{j=1}^k \mathbf{L}_j \mathbf{L}_T. \tag{A2}$$

In this expression, the incident transfer matrix L_I^{-1} projects the incident electromagnetic plane wave onto the sample's surface, and the exit transfer matrix L_T projects the transmitted wave components onto the substrate. The second factor encapsulates the properties of the various layers within the sample, with k representing the total number of layers. The transfer matrix for each individual layer can be expressed as

$$\mathbf{L}_{j} = \exp\left(-i\frac{\omega\hat{\Delta}d}{c}\right),\tag{A3}$$

where c is the speed of light in vacuum, ω is the frequency of the electromagnetic wave, d the thickness of the sample. The $\hat{\Delta}$ matrix is derived directly from Maxwell's equations and contains elements of the permeability and permittivity tensor in the frequency domain expansion:

$$\begin{pmatrix}
\mu_{yx} - \frac{\mu_{yz}\mu_{zx}}{\mu_{zz}} & -q_x^2 \frac{1}{\varepsilon_{zz}} + \mu_{yy} - \frac{\mu_{yz}\mu_{zy}}{\mu_{zz}} \\
-\mu_{xx} + \frac{\mu_{xz}\mu_{zx}}{\mu_{zz}} & -\mu_{xy} + \frac{\mu_{xz}\mu_{zy}}{\mu_{zz}} \\
-q_x \frac{\mu_{zx}}{\mu_{zz}} & q_x \left(\frac{\varepsilon_{yz}}{\varepsilon_{zz}} - \frac{\mu_{zy}}{\mu_{zz}}\right) \\
0 & -q_x \frac{\varepsilon_{xz}}{\varepsilon_{zz}}
\end{pmatrix}, (A4)$$

 $M_{23,32}$ are proportional to the circular birefringence caused by the spin transitions [29]. Consequently, the Mueller matrix elements $M_{23,32}$ and $M_{14,41}$ are employed for the detection of EPR signals in this study. These elements can be written in the form of transfer matrix elements $L_{k,l}$ with k, l = 1, 2, 3, 4:

$$\begin{split} M_{23} &= \text{Re} \left(\frac{(L_{11}L_{43} - L_{13}L_{41})(L_{11}L_{23} - L_{13}L_{21})^*}{L_{11}L_{33} - L_{13}L_{31}} - \frac{(L_{33}L_{21} - L_{31}L_{23})(L_{33}L_{41} - L_{31}L_{43})^*}{L_{11}L_{33} - L_{13}L_{31}} \right), \quad \text{(B1)} \\ M_{32} &= \text{Re} \left(\frac{(L_{11}L_{43} - L_{13}L_{41})(L_{33}L_{41} - L_{31}L_{43})^*}{L_{11}L_{33} - L_{13}L_{31}} - \frac{(L_{33}L_{21} - L_{31}L_{23})(L_{11}L_{23} - L_{13}L_{21})^*}{L_{11}L_{33} - L_{13}L_{31}} \right), \quad \text{(B2)} \\ M_{14} &= \text{Im} \left(\frac{(L_{11}L_{43} - L_{13}L_{41})(L_{11}L_{23} - L_{13}L_{21})^*}{L_{11}L_{33} - L_{13}L_{31}} - \frac{(L_{33}L_{21} - L_{31}L_{23})(L_{33}L_{41} - L_{31}L_{43})^*}{L_{11}L_{33} - L_{13}L_{31}} \right), \quad \text{(B3)} \end{split}$$

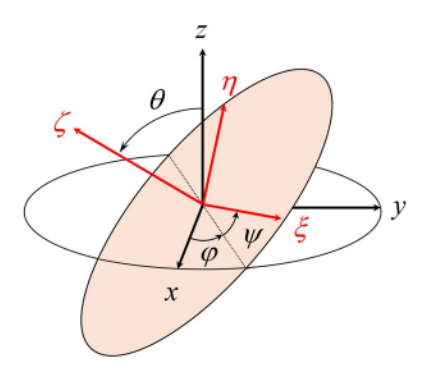


FIG. 6. Definition of the Euler angles φ , θ , and ψ and the orthogonal rotations as provided by A. (ξ, η, ζ) , and (x, y, z) refer to the Cartesian auxiliary and laboratory coordinate systems, respectively. Reprinted from Ref. [34] with copyright permission by American Physical Society.

and

$$M_{41} = \operatorname{Im}\left(\frac{(L_{11}L_{43} - L_{13}L_{41})(L_{33}L_{41} - L_{31}L_{43})^*}{L_{11}L_{33} - L_{13}L_{31}} - \frac{(L_{33}L_{21} - L_{31}L_{23})(L_{11}L_{23} - L_{13}L_{21})^*}{L_{11}L_{33} - L_{13}L_{31}}\right), \quad (B4)$$

where * symbolizes complex conjugate. From these expressions, it is evident that M14 and M23 are the imaginary and real part of the same function, respectively, and the same holds true for M41 and M32.

1. Euler rotations

For a given magnetic field orientation, Euler angle rotations are required to bring μ into the correct appearance within the ellipsometer system (x, y, z). Euler rotations which perform

such operations are shown in Fig. 6. Operation $R_1(v=\phi)$ renders rotation around z, $R_2(v=\theta)$ around x, and $R_1(v=\psi)$ around new direction ζ with mathematically positive (negative) sense for positive (negative) arguments

$$R_1(v) = \begin{pmatrix} \cos v & -\sin v & 0\\ \sin v & \cos v & 0\\ 0 & 0 & 1 \end{pmatrix},$$
 (B5)

$$R_2(v) = \begin{pmatrix} 1 & 0 & 0 \\ 0 & \cos v & -\sin v \\ 0 & \sin v & \cos v \end{pmatrix}.$$
 (B6)

The full set of rotations, φ , θ , ψ indicated in Fig. 6, is then described by matrix A

$$A = R_1(\varphi)R_2(\theta)R_1(\psi), \tag{B7}$$

where $\hat{\mu}$ indicates the tensor appearance of μ in a new auxiliary system

$$\hat{\mu} = A\mu A^{-1}. (B8)$$

Due to the rotational invariance of Eq. (27) around its gyration vector in Eq. (28) rotation $R_1(\psi)$ is not needed for addressing the magnetic field direction relative to the sample system within the ellipsometer system. However, the rotational dependencies of the Hamiltonian parameters will depend on the sample orientation relative to the ellipsometer system and the magnetic field direction. For proper sample rotation to align the dielectric tensor within the ellipsometer system, all three Euler rotations maybe necessary.

^[1] C. Poole, Electron Spin Resonance: A Comprehensive Treatise on Experimental Techniques (Wiley, New York, 1983).

^[2] S. Rast, A. Borel, L. Helm, E. Belorizky, P. H. Fries, and A. E. Merbach, EPR spectroscopy of MRI-related Gd(III) complexes: Simultaneous analysis of multiple frequency and temperature spectra, including static and transient crystal field effects, J. Am. Chem. Soc. 123, 2637 (2001).

^[3] F. Bloch, Nuclear induction, Phys. Rev. 70, 460 (1946).

^[4] A. Savitsky and K. Möbius, High-field EPR, Photosynth. Res. 102, 311 (2009).

^[5] P. Neugebauer, D. Bloos, R. Marx, P. Lutz, M. Kern, D. Aguilà, J. Vaverka, O. Laguta, C. Dietrich, R. Clérac, and J. van Slageren, Ultra-broadband EPR spectroscopy in field and frequency domains, Phys. Chem. Chem. Phys. 20, 15528 (2018).

^[6] O. Laguta, M. Tucek, J. van Slageren, and P. Neugebauer, Multi-frequency rapid-scan HFEPR, J. Mag. Res. 296, 138 (2018).

^[7] A. L. Barra, A. Caneschi, D. Gatteschi, and R. Sessoli, High-frequency EPR spectra for the analysis of magnetic anisotropy in large magnetic clusters, J. Am. Chem. Soc. 117, 8855 (1995).

^[8] A. K. Hassan, L. A. Pardi, J. Krzystek, A. Sienkiewicz, P. Goy, M. Rohrer, and L. C. Brunel, Ultrawide band multifrequency

high-field EMR technique: A methodology for increasing spectroscopic information, J. Mag. Res. 142, 300 (2000).

^[9] F. F. Murzakhanov, B. V. Yavkin, G. V. Mamin, S. B. Orlinskii, H. J. von Bardeleben, T. Biktagirov, U. Gerstmann, and V. A. Soltamov, Hyperfine and nuclear quadrupole splitting of the NV⁻ ground state in 4*H*-SiC, Phys. Rev. B 103, 245203 (2021).

^[10] K. Szász, X. T. Trinh, N. T. Son, E. Janzén, and A. Gali, Theoretical and electron paramagnetic resonance studies of hyperfine interaction in nitrogen doped 4H and 6H SiC, J. Appl. Phys. 115, 073705 (2014).

^[11] N. T. Son, J. Isoya, T. Umeda, I. G. Ivanov, A. Henry, T. Ohshima, and E. Janzén, EPR and ENDOR studies of shallow donors in SiC, Appl. Mag. Res. 39, 49 (2010).

^[12] M. E. Zvanut, S. Paudel, E. R. Glaser, M. Iwinska, T. Sochacki, and M. Bockowski, Incorporation of carbon in free-standing HVPE-grown GaN substrates, J. Elec. Mat. 48, 2226 (2019).

^[13] U. R. Sunay, M. E. Zvanut, J. Marbey, S. Hill, J. H. Leach, and K. Udwary, Small non-uniform basal crystal fields in HVPE free-standing GaN:Mg as evidenced by angular dependent and frequency-dependent EPR, J. Phys.: Condens. Matter 31, 345702 (2019).

- [14] B. E. Kananen, L. E. Halliburton, E. M. Scherrer, K. T. Stevens, G. K. Foundos, K. B. Chang, and N. C. Giles, Electron paramagnetic resonance study of neutral Mg acceptors in β-Ga₂O₃ crystals, Appl. Phys. Lett. 111, 072102 (2017).
- [15] H. J. von Bardeleben, S. Zhou, U. Gerstmann, D. Skachkov, W. R. L. Lambrecht, Q. D. Ho, and P. Deák, Proton irradiation induced defects in β-Ga₂O₃: A combined EPR and theory study, APL Mat. 7, 022521 (2019).
- [16] N. T. Son, K. Goto, K. Nomura, Q. T. Thieu, R. Togashi, H. Murakami, Y. Kumagai, A. Kuramata, M. Higashiwaki, A. Koukitu, S. Yamakoshi, B. Monemar, and E. Janzén, Electronic properties of the residual donor in unintentionally doped β-Ga₂O₃, J. Appl. Phys. 120, 235703 (2016).
- [17] C. A. Lenyk, T. D. Gustafson, S. A. Basun, L. E. Halliburton, and N. C. Giles, Experimental determination of the (0/-) level for Mg acceptors in β-Ga₂O₃ crystals, Appl. Phys. Lett. 116, 142101 (2020).
- [18] C. A. Lenyk, T. D. Gustafson, L. E. Halliburton, and N. C. Giles, Deep donors and acceptors in β-Ga₂O₃ crystals: Determination of the Fe^{2+/3+} level by a noncontact method, J. Appl. Phys. 126, 245701 (2019).
- [19] J. E. Stehr, D. M. Hofmann, J. Schörmann, M. Becker, W. M. Chen, and I. A. Buyanova, Electron paramagnetic resonance signatures of Co²⁺ and Cu²⁺ in β-Ga₂O₃, Appl. Phys. Lett. 115, 242101 (2019).
- [20] C. A. Lenyk, N. C. Giles, E. M. Scherrer, B. E. Kananen, L. E. Halliburton, K. T. Stevens, G. K. Foundos, J. D. Blevins, D. L. Dorsey, and S. Mou, Ir⁴⁺ ions in β-Ga₂O₃ crystals: An unintentional deep donor, J. Appl. Phys. 125, 045703 (2019).
- [21] N. T. Son, Q. D. Ho, K. Goto, H. Abe, T. Ohshima, B. Monemar, Y. Kumagai, T. Frauenheim, and P. Deák, Electron paramagnetic resonance and theoretical study of gallium vacancy in β-Ga₂O₃, Appl. Phys. Lett. 117, 032101 (2020).
- [22] J. Lu, I. O. Ozel, C. A. Belvin, X. Li, G. Skorupskii, L. Sun, B. K. Ofori-Okai, M. Dincă, N. Gedik, and K. A. Nelson, Rapid and precise determination of zero-field splittings by terahertz time-domain electron paramagnetic resonance spectroscopy, Chem. Sci. 8, 7312 (2017).
- [23] J. Krzystek, S. A. Zvyagin, A. Ozarowski, S. Trofimenko, and J. Telser, en Tunable-frequency high-field electron paramagnetic resonance, J. Magn. Reson. 178, 174 (2006).
- [24] C. Bray, K. Maussang, C. Consejo, J. A. Delgado-Notario, S. Krishtopenko, I. Yahniuk, S. Gebert, S. Ruffenach, K. Dinar, E. Moench, J. Eroms, K. Indykiewicz, B. Jouault, J. Torres, Y. M. Meziani, W. Knap, A. Yurgens, S. D. Ganichev, and F. Teppe, Temperature-dependent zero-field splittings in graphene, Phys. Rev. B 106, 245141 (2022).
- [25] E. Ohmichi, Y. Shoji, H. Takahashi, and H. Ohta, Frequency-domain electron spin resonance spectroscopy using continuously frequency-tunable terahertz photomixers, Appl. Phys. Lett. 119, 162404 (2021).
- [26] P. Kühne, C. M. Herzinger, M. Schubert, J. A. Woollam, and T. Hofmann, Invited article: An integrated mid-infrared, farinfrared, and terahertz optical Hall effect instrument, Rev. Sci. Instr. 85, 071301 (2014).
- [27] P. Kühne, N. Armakavicius, V. Stanishev, C. M. Herzinger, M. Schubert, and V. Darakchieva, Advanced terahertz frequency-domain ellipsometry instrumentation for in situ and ex situ applications, IEEE Trans. Terahertz Sci. Technol. 8, 257 (2018).

- [28] S. Knight, S. Schöche, P. Kühne, T. Hofmann, V. Darakchieva, and M. Schubert, Tunable cavity-enhanced terahertz frequencydomain optical Hall effect, Rev. Sci. Instr. 91, 083903 (2020).
- [29] M. Schubert, S. Knight, S. Richter, P. Kühne, V. Stanishev, A. Ruder, M. Stokey, R. Korlacki, K. Irmscher, P. Neugebauer, and V. Darakchieva, Terahertz electron paramagnetic resonance generalized spectroscopic ellipsometry: The magnetic response of the nitrogen defect in 4H-SiC, Appl. Phys. Lett 120, 102101 (2022).
- [30] A. Kimel, A. Zvezdin, S. Sharma, S. Shallcross, N. de Sousa, A. García-Martín, G. Salvan, J. Hamrle, O. Stejskal, J. McCord, S. Tacchi, G. Carlotti, P. Gambardella, G. Salis, M. Münzenberg, M. Schultze, V. Temnov, I. V. Bychkov, L. N. Kotov, N. Maccaferri, D. Ignatyeva, V. Belotelov, C. Donnelly, A. H. Rodriguez, I. Matsuda, T. Ruchon, M. Fanciulli, M. Sacchi, C. R. Du, H. Wang, N. P. Armitage, M. Schubert, V. Darakchieva, B. Liu, Z. Huang, B. Ding, A. Berger, and P. Vavassori, The 2022 magneto-optics roadmap, J. Phys. D: Appl. Phys. 55, 463003 (2022).
- [31] J. A. Weil and J. R. Bolton, Electron Paramagnetic Resonance Elementary Theory and Practical Applications (John Wiley & Sons, Hoboken, New Jersey, 2007).
- [32] S. Richter, S. Knight, O. Bulancea-Lindvall, S. Mu, P. Kühne, M. Stokey, A. Ruder, V. Rindert, V. Ivády, I. A. Abrikosov, C. G. Van de Walle, M. Schubert, and V. Darakchieva, High-field/high-frequency electron spin resonances of Fe-doped β-Ga₂O₃ by terahertz generalized ellipsometry: Monoclinic symmetry effects, Phys. Rev. B 109, 214106 (2024).
- [33] Principles of optics, in *Spectroscopic Ellipsometry* (John Wiley & Sons, Ltd, Hoboken, New Jersey, 2007), Chap. 2, 3, 4, pp. 13–207.
- [34] M. Schubert, R. Korlacki, S. Knight, T. Hofmann, S. Schöche, V. Darakchieva, E. Janzén, B. Monemar, D. Gogova, Q.-T. Thieu, R. Togashi, H. Murakami, Y. Kumagai, K. Goto, A. Kuramata, S. Yamakoshi, and M. Higashiwaki, Anisotropy, phonon modes, and free charge carrier parameters in monoclinic β-gallium oxide single crystals, Phys. Rev. B 93, 125209 (2016).
- [35] A. Mock, R. Korlacki, S. Knight, and M. Schubert, Anisotropy, phonon modes, and lattice anharmonicity from dielectric function tensor analysis of monoclinic cadmium tungstate, Phys. Rev. B 95, 165202 (2017).
- [36] M. Schubert, Coordinate-invariant lyddane-sachs-teller relationship for polar vibrations in materials with monoclinic and triclinic crystal systems, Phys. Rev. Lett. 117, 215502 (2016).
- [37] A. Mock, R. Korlacki, S. Knight, and M. Schubert, Anisotropy and phonon modes from analysis of the dielectric function tensor and the inverse dielectric function tensor of monoclinic yttrium orthosilicate, Phys. Rev. B 97, 165203 (2018).
- [38] A. Mock, R. Korlacki, S. Knight, M. Stokey, A. Fritz, V. Darakchieva, and M. Schubert, Lattice dynamics of orthorhom-bic NdGaO₃, Phys. Rev. B 99, 184302 (2019).
- [39] M. Schubert, A. Mock, R. Korlacki, and V. Darakchieva, Phonon order and reststrahlen bands of polar vibrations in crystals with monoclinic symmetry, Phys. Rev. B 99, 041201(R) (2019).
- [40] M. Schubert, A. Mock, R. Korlacki, S. Knight, Z. Galazka, G. Wagner, V. Wheeler, M. Tadjer, K. Goto, and V. Darakchieva, Longitudinal phonon plasmon mode coupling in β-Ga₂O₃, Appl. Phys. Lett. 114, 102102 (2019).

- [41] H. S. Gutowsky and C. H. Holm, Rate processes and nuclear magnetic resonance Spectra. II. hindered internal rotation of amides, J. Chem. Phys. 25, 1228 (1956).
- [42] H. M. McConnell, Reaction rates by nuclear magnetic resonance, J. Chem. Phys. 28, 430 (1958).
- [43] R. Berger, J.-C. Bissey, J. Kliava, R. Berger, and J.-C. Bissey, Lineshapes in magnetic resonance spectra, J. Phys.: Condens. Matter 12, 9347 (2000).
- [44] P. W. Percival and J. S. Hyde, Pulsed EPR spectrometer, II, Rev. Sci. Instrum. 46, 1522 (1975).
- [45] S. R. P. Smith, F. Dravnieks, and J. E. Wertz, Electron-paramagnetic-resonance line shape of Ni²⁺ in MgO, Phys. Rev. 178, 471 (1969).
- [46] Z. Soskic, B. B. Stojic, and M. Stojic, Electron paramagnetic resonance studies of Zn_{1-x}Mn_xTe, J. Phys.: Condens. Matter 6, 1261 (1994).
- [47] S. S. Eaton and G. R. Eaton, Relaxation times of organic radicals and transition metal ions, in *Distance Measurements in Biological Systems by EPR*, edited by L. J. Berliner, G. R. Eaton, and S. S. Eaton (Springer US, Boston, MA, 2000), pp. 29–154.
- [48] H. Mueller, Memorandum on the polarization optics of the photoelastic shutter, Report of the OSRD project OEMsr-576 2 (Massachusets Institute of Technology, Cambridge, Massachusetts, 1943).
- [49] J. N. Hilfiker, N. Hong, and S. Schoeche, Mueller matrix spectroscopic ellipsometry, Adv. Opt. Technol. 11, 59 (2022).
- [50] M. Schubert, P. Kühne, V. Darakchieva, and T. Hofmann, Optical Hall effect—model description: tutorial, J. Opt. Soc. Am. A 33, 1553 (2016).
- [51] T. Kashiwagi, S. Sonoda, H. Yashiro, Y. Ishihara, A. Usui, Y. Akasaka, and M. Hagiwara, Electron spin resonance in GaN thin film doped with Fe, Jpn. J. Appl. Phys. 46, 581 (2007).
- [52] C. P. Slichter, Basic theory, in *Principles of Magnetic Resonance* (Springer, Berlin, Heidelberg, Berlin, Heidelberg, 1990), pp. 11–64.
- [53] J. A. Weil and J. R. Bolton, Relaxation times, linewidths and spin kinetic phenomena, in *Electron Paramagnetic Resonance* (John Wiley & Sons, Ltd, Hoboken, New Jersey, 2006), Chap. 10, pp. 301–356.
- [54] Note that this step was omitted in the ad-hoc model function approach in Ref. [29] leading to unphysical behaviors of the resulting tensor at low frequencies where the off-diagonal components do not vanish but should.
- [55] J. D. Jackson, Classical Electrodynamics, 3rd ed. (John Wiley & Sons, New York, NY, 1999).
- [56] J. de Rosny, G. Lerosey, A. Tourin, and M. Fink, Time reversal of electromagnetic waves, in *Modeling and Computations in Electromagnetics*, edited by H. Ammari (Springer, Berlin, Heidelberg, 2008), pp. 187–202.
- [57] O. Sigwarth and C. Miniatura, Time reversal and reciprocity, AAPPS Bulletin 32, 23 (2022).
- [58] S. Stoll and A. Schweiger, Easyspin, a comprehensive software package for spectral simulation and analysis in EPR, J. Magn. Reson. 178, 42 (2006).
- [59] J. Pilbrow, Lineshapes in frequency-swept and field-swept EPR for spin 12, J. Magn. Reson. (1969) 58, 186 (1984).
- [60] M. Born and K. Huang, Dynamical theory of Crystal Lattices (Clarendon Press, Oxford, 1954).
- [61] M. Stokey, A. Mock, R. Korlacki, S. Knight, V. Darakchieva, S. Schöche, and M. Schubert, Infrared active phonons in mon-

- oclinic lutetium oxyorthosilicate, J. Appl. Phys. 127, 115702 (2020).
- [62] N. C. Passler, X. Ni, G. Hu, J. R. Matson, G. Carini, M. Wolf, M. Schubert, A. Alù, J. D. Caldwell, T. G. Folland, and A. Paarmann, Hyperbolic shear polaritons in low-symmetry crystals, Nature (London) 595, 1476 (2022).
- [63] A. Mock, R. Korlacki, C. Briley, V. Darakchieva, B. Monemar, Y. Kumagai, K. Goto, M. Higashiwaki, and M. Schubert, Band-to-band transitions, selection rules, effective mass, and excitonic contributions in monoclinic β—Ga₂O₃, Phys. Rev. B 96, 245205 (2017).
- [64] Note that $vA^{-1} = (A^{-1})^T v = Av$, when A is a unitary matrix, i.e., $AA^{-1} = AA^T = I$ and I is the unit matrix and v a vector.
- [65] When the eigenvectors are not equal, i.e., when the gyration vectors differ among the j resonances, then the response functions are projected onto the permeability tensor components and require further analysis.
- [66] P. Baranov, I. Ilyin, and E. Mokhov, Identification of iron transition group trace impurities in gan bulk crystals by electron paramagnetic resonance, Solid State Commun. 101, 611 (1997).
- [67] K. Maier, M. Kunzer, U. Kaufmann, J. Schneider, B. Monemar, I. Akasaki, and H. Amano, Iron acceptors in gallium nitride (gan), in *Defects in Semiconductors 17*, Materials Science Forum, Vol. 143 (Trans Tech Publications Ltd, Bäch, Switzerland, 1993), pp. 93–98.
- [68] B. Bleaney and R. S. Trenam, Paramagnetic resonance spectra of some ferric alums, and the nuclear magnetic moment of ⁵⁷Fe, Proc. R. Soc. London A 223, 1 (1954).
- [69] S. Geschwind, Paramagnetic resonance of Fe³⁺ in octahedral and tetrahedral sites in yttrium gallium garnet (YGaG) and anisotropy of yttrium iron garnet (YIG), Phys. Rev. 121, 363 (1961).
- [70] K. Momma and F. Izumi, VESTA3 for three-dimensional visualization of crystal, volumetric and morphology data, J. Appl. Crystal. 44, 1272 (2011).
- [71] A. G. Maryasov and M. K. Bowman, Bloch equations for anisotropic paramagnetic centers with spin of 1/2, J. Magn. Reson. 233, 80 (2013).
- [72] T. Paskova, R. Kroeger, S. Figge, D. Hommel, V. Darakchieva, B. Monemar, E. Preble, A. Hanser, N. M. Williams, and M. Tutor, High-quality bulk a-plane GaN sliced from boules in comparison to heteroepitaxially grown thick films on r-plane sapphire, Appl. Phys. Lett. 89, 051914 (2006).
- [73] M.-Y. Xie, N. Ben Sedrine, S. Schöche, T. Hofmann, M. Schubert, L. Hung, B. Monemar, X. Wang, A. Yoshikawa, K. Wang, T. Araki, Y. Nanishi, and V. Darakchieva, Effect of Mg doping on the structural and free-charge carrier properties of InN films, J. Appl. Phys. 115, 163504 (2014).
- [74] V. Darakchieva, B. Monemar, A. Usui, M. Saenger, and M. Schubert, Lattice parameters of bulk GaN fabricated by halide vapor phase epitaxy, J. Cryst. Growth 310, 959 (2008), proceedings of the E-MRS Conference, Symposium G.
- [75] A. Ruder, B. Wright, R. Feder, U. Kilic, M. Hilfiker, E. Schubert, C. M. Herzinger, and M. Schubert, Mueller matrix imaging microscope using dual continuously rotating anisotropic mirrors, Opt. Express 29, 28704 (2021).
- [76] A. Ruder, B. Wright, D. Peev, R. Feder, U. Kilic, M. Hilfiker, E. Schubert, C. M. Herzinger, and M. Schubert, Mueller matrix ellipsometer using dual continuously rotating anisotropic mirrors, Opt. Lett. 45, 3541 (2020).

- [77] T. Hofmann, D. Schmidt, A. Boosalis, P. Kühne, R. Skomski, C. M. Herzinger, J. A. Woollam, M. Schubert, and E. Schubert, THz dielectric anisotropy of metal slanted columnar thin films, Appl. Phys. Lett. 99, 081903 (2011).
- [78] T. Hofmann, D. Schmidt, and M. Schubert, Thz generalized ellipsometry characterization of highly-ordered threedimensional nanostructures, in *Ellipsometry at the Nanoscale*, edited by M. Losurdo and K. Jingerl (Springer, Verlag, Berlin, Heidelberg, 2013), Chap. 11, pp. 411–428.
- [79] D. W. Berreman, Optics in stratified and anisotropic media: 4×4-matrix formulation, J. Opt. Soc. Am. 62, 502 (1972).
- [80] M. Schubert, Polarization-dependent optical parameters of arbitrarily anisotropic homogeneous layered systems, Phys. Rev. B 53, 4265 (1996).
- [81] M. Hibberd, V. Frey, B. Spencer, P. Mitchell, P. Dawson, M. Kappers, R. Oliver, C. Humphreys, and D. Graham, Dielectric response of wurtzite gallium nitride in the terahertz frequency range, Solid State Commun. 247, 68 (2016).
- [82] P. Virtanen, R. Gommers, T. E. Oliphant, M. Haberland, T. Reddy, D. Cournapeau, E. Burovski, P. Peterson, W. Weckesser, J. Bright, S. J. van der Walt, M. Brett, J. Wilson, K. J. Millman, N. Mayorov, A. R. J. Nelson, E. Jones, R. Kern, E. Larson, C. J. Carey, İ. Polat, Y. Feng, E. W. Moore, J. VanderPlas, D. Laxalde, J. Perktold, R. Cimrman, I. Henriksen, E. A. Quintero, C. R. Harris, A. M. Archibald, A. H. Ribeiro, F. Pedregosa, P. van Mulbregt, and SciPy 1.0 Contributors, SciPy 1.0: Fundamental algorithms for scientific computing in python, Nature Methods 17, 261 (2020).

- [83] A diagram of the magnetic field distribution within the sample plane is shown in the supplementary material in Ref. [29].
- [84] O. Arteaga and R. Ossikovski, Mueller matrix analysis, decompositions, and novel quantitative approaches to processing complex polarimetric data, in *Polarized Light in Biomedical Imaging and Sensing: Clinical and Preclinical Applications*, edited by J. C. Ramella-Roman and T. Novikova (Springer International Publishing, Cham, 2023), pp. 25–60.
- [85] N. Bloembergen, On the interaction of nuclear spins in a crystalline lattice, Physica 15, 386 (1949).
- [86] T. Gilbert, A phenomenological theory of damping in ferromagnetic materials, IEEE Trans. Magn. 40, 3443 (2004).
- [87] L. Landau and E. Lifshitz, 3 on the theory of the dispersion of magnetic permeability in ferromagnetic bodiesreprinted from physikalische zeitschrift der sowjetunion 8, part 2, 153, 1935, in *Perspectives in Theoretical Physics*, edited by L. Pitaevski (Pergamon, Amsterdam, 1992) pp. 51–65.
- [88] M. Lakshmanan, The fascinating world of the landau-lifshitzgilbert equation: an overview, Philos. Trans. R. Soc. A 369, 1280 (2011).
- [89] D. Hoult, The solution of the bloch equations in the presence of a varying b1 field—an approach to selective pulse analysis, J. Magn. Reson. (1969) 35, 69 (1979).
- [90] T. Prisner, M. Rohrer, and F. MacMillan, Pulsed EPR spectroscopy: Biological applications, Annu. Rev. Phys. Chem. 52, 279 (2001).
- [91] P. Yeh, Electromagnetic propagation in birefringent layered media, J. Opt. Soc. Am. 69, 742 (1979).